NTNU – Trondheim
Norwegian University of
Science and Technology

TEM characterization of Cr-doped ZnS Thin Films for Solar Cell applications

Eivind Seim

In memory of my dear friend Lars Olav..

Abstract

The morphology of three Cr-doped zinc sulfide thin films, one deposited by molecular beam epitaxy (MBE) and two by pulsed laser deposition (PLD), have been studied by transmission electron microscopy (TEM). Investigations of the polymorphic crystal structure of ZnS have been done by analysis of diffraction, bright field and high resolution images. Both similarities and differences in morphology between the three samples have been discovered. An unambiguous determination of the crystal structure could not be done due to the similarities of the possible phases of ZnS. However, evidence show that the MBE sample contains more zinc blende than wurtzite, and that the PLD samples are containing more wurtzite than zinc blende. It is also found that the cross section PLD sample is textured in the growth direction of the film. The MBE sample does not show this texture, but here twin stacking faults are commonly found.

The cross section PLD sample was studied in greater detail using energy-dispersive X-ray spectroscopy (EDX) and electron energy loss spectroscopy (EELS). EDX analysis revealed relatively large variations in Cr concentration, and a connection between increases in Cr and decreases in Zn was discovered, indicating that Cr is substituting Zn in the ZnS lattice. Determination of the valence state of Cr was done by EELS analysis, and found to be +II, a result supporting the indications of the EDX analysis.

ZnS:Cr is an interesting material for realizing the intermediate band solar cell concept using ultrahigh doping levels. Still, the three samples show that the material is underdeveloped at this stage for solar cells, as the thin films are polycrystalline with small grains, and have features that increase recombination.

Samandrag

Morfologien til tre Cr-dopa tynnfilmar av sinksulfid, deponert med molekyl-stråleepitaksi (MBE) og pulsa laserdeponering (PLD), har blitt studert med transmisjonelektronmikroskop (TEM). Den polymorfe krystallstrukturen til ZnS har blitt undersøkt ved å analysere diffraksjons-, ljosfelt- og høgoppløysingsbilete. Morfologiske likskapar og ulikskapar har blitt funne mellom dei tre prøvane. Å gje ei eintydig skildring av krystallstrukturen har ikkje lete seg gjere på grunn av likskapane mellom dei moglege fasane til ZnS. Det har likevel blitt funne belegg for at krystallstrukturen til MBE-prøven er meir sinkblende enn wurtzitt, og at PLD-prøvane er wurtzitt enn sinkblende. Det er og funne at tversnitt PLD-prøva er teksturert i groretninga til filmen. MBE-prøva har ikkje denne teksturen, men i denne er det vanleg å finne tvillingstablefeil i korna.

Ei PLD prøve blei studert i detalj med røntgenspektroskopi (EDX) og elektron energitap spektroskopi (EELS). EDX-analyse synte store variasjonar i Cr-konsentrasjon, og ein samanheng mellom auking i Cr og minking i Zn blei oppdaga, noko som indikerer at Cr substituerer Zn i ZnS-gitteret. Valenstilstanden til Cr blei bestemt ved hjelp av EELS-analyse, og funnen til å vere +II, eit resultat som støttar indikasjonane frå EDX-analysen.

ZnS:Cr er eit interessant materiale for solcellekonseptet med mellomband ved ultrahøge dopingnivå. Trass i dette syner dei tre prøvane at materialet er under-utvikla for bruk i solceller på grunn av at tynnfilmane er polykrystallinske med små korn og har trekk som aukar rekombinasjon.

Preface

This thesis documents the work done during my Master's degree studies in physics at the Norwegian University of Science and Technology, NTNU. The project has been done at the Department of Physics with Randi Holmestad as supervisor and Turid Worren Reenaas as co-supervisor.

I would like to thank Randi Holmestad for giving me supervision and interesting discussions, Turid Worren Reenaas, Mohammadreza Nematollahi and Xiaodong Yang for providing the samples that I have studied, and Per Erik Vullum, Ragnhild Sæterlid, Ton van Helvoort and Bjørn Soleim for always helping me out and giving me advice on TEM and sample preparation. I would also like to thank everyone in the TEM group.

A special thanks goes out to my wife Anja, my friends and family, for always being there for me.

Trondheim, May 2014

Eivind Seim

List of Abbreviations

CB   Conduction Band of semiconductor

DM   Gatan Digital Micrograph

EDX   Energy-Dispersive X-ray Spectroscopy

EELS   Electron Energy Loss Spectroscopy

EQE   External quantum efficiency

FEG   Field Emission Gun

FWHM   Full Width at Half Maximum

HRTEM   High Resolution Transmission Electron Microscopy

IBSC   Intermediate Band Solar Cell

IB   Intermediate Band

IQE   Internal quantum efficiency

MBE   Molecular Beam Epitaxy

PLD   Pulsed Laser Deposition

SEM   Scanning Electron Microscopy

SRH   Shockley-Read-Hall

STEM   Scanning Transmission Electron Microscopy

TEM   Transmission Electron Microscope

UHD-IBSC   Ultrahigh Doping Intermediate Band Solar Cell

VB   Valence Band of semiconductor

VLM   Visual Light Microscope

XRD   X-Ray Diffraction

ZnS:Cr   Chromium doped zinc sulfide

Sample Naming Convention

A naming convention was made to make it easier for the reader to keep track of the deposition technique and preparation method used for a given sample. All three samples, which are Cr-doped ZnS, are abbreviated xZnS:Cry. In this convention x is used to denote deposition technique, "P" for PLD and "M" for MBE, while y is used to denote the preparation method used, "CS" for cross section and "PV" for plan view. An example of use is MZnS:CrCS which means a Cr-doped ZnS sample grown by MBE and prepared to be studied in cross section.

Contents

Chapter 1

Introduction

As the world's population grows larger and larger, so does our need for energy in order to keep up with advances in living standards and technology. The US Energy Information Administration estimates that the world's demand for energy will continue to increase in the years to come [1]. We are facing an important problem when trying to meet the increasing demand of energy. How do we produce more energy in a way that is sustainable for our environment? Today, a significant amount of the total energy production is generated by burning fossil fuels which is releasing CO_2 into the atmosphere. It is widely accepted in the scientific community that our climate is undergoing a change at a rapid pace [2]. An explanation to this is the green-house effect of CO_2. The projected consequences of climate change on this scale are severe [3]. More extreme weather, drought, extinction and tougher conditions for food production are some outcomes. Fossil fuels are not a renewable source of energy and will eventually be depleted, but the need of energy will still be there.

To cover our needs of energy, other energy sources must be exploited to a greater extent. Ideally, this source should be safe, renewable, environmentally friendly, and reliable. The sun is an energy source fit for this description. Only a small fraction of the energy that shines on the earth every second is enough to cover our entire energy demand. Needless to say, solar cells have a vast potential, but so is the challenge to be overcome. The efficiency of the energy harvest needs to be better and cheaper than what is status quo. This is both to achieve grid parity and to be area effective. A lot of efforts have been put into the research of more efficient solar cells. New concepts like intermediate band solar cells (IBSC) have been reported to have the potential to perform better than conventional solar cells [4].

1.1 The Project

Microstructure has a large impact on the performance of a solar cell. Every imperfection in the material will decrease the efficiency of the energy conversion. The ideal situation would be to have crystalline ZnS with Cr distributed evenly throughout the thin film, but this is yet to be achieved. In order to improve the quality thin films, more knowledge about the current ones are needed. The ZnS thin films studied are deposited by different means and may have different microstructural properties. Therefore, the scope of this study is to characterize the microstructure in ZnS thin films and to find out how Cr is distributed in the Cr-doped samples using a range of techniques available in TEM. It is also of interest to investigate if there are any notable differences between the samples and to see if it is possible to relate it to the deposition technique.

The thesis is divided into four main chapters: A theory chapter covering relevant topics to give the reader a foundation to understand the rest of the thesis; a chapter covering the experimental work that has been done, described in detail for reproducibility; a chapter presenting the results and findings during the work on the project; and a chapter discussing the results with a critical eye to errors and factors that might create misleading results.

Chapter 2

Theory

2.1   Solar Cells

Solar cell technology is advancing as a green and reliable source of energy. Silicon based single junction solar cells are by far the most developed technology and the most widespread. Still, there is much to gain by developing new solar cells with potentially higher efficiency. Quite a few concepts are being explored and researched in order to make solar cells more competitive to fossil fuels.

The different types of solar cell technology are divided into three groups, or generations as they are commonly called. The first generation solar cells are high quality crystalline silicon single junction cells. These cells use very pure silicon to have the least amount of defects in the crystal. Even if the costs are high to produce these cells, they are the most commercially attractive due to price per kWh.

The second generation solar cells are an effort to make the principles from the first generation cheaper. This is done by using thin film technologies, polymers and organic materials. Materials commonly used are cadmium telluride (CdTe), cadmium indium gallium selenide (CIGS) and amorphous silicon.

The third generation solar cells aim for better efficiency than the first and second generation by using new concepts. Some of the new concepts are hot-carrier cells, cells with multiple charge carriers per absorbed photon, multiple bandgap cells and intermediate bandgap cells. These new concepts have a much higher theoretical efficiency, some with up to 86.8%, compared to 40.7% efficiency for a single junction cell [5].

2.1.1 The Photovoltaic Effect and the PN-junction

The basic principle for all solar cells is the photovoltaic effect. In a semiconducting material, incoming radiation of sufficient energy can excite electrons from the valence band (VB) into the conduction band (CB). This process creates two charge carriers, an electron and a hole, and will only happen if the incoming photon has energy greater or equal to the bandgap energy E_g.

The photovoltaic effect wouldn't do much on its own for solar cells without the PN-juction. A PN-junction is a device that separates charges created by the photovoltaic effect. It is formed at the interface of two types of semiconducting materials, referred to as N-type and P-type, Fig. 2.1. In the case of a silicon based PN-junction, the N-type is silicon doped with an element that has more electrons than silicon, usually phosphorus. The phosphorus "donates" an electron to the N-type and makes it act like an electron membrane. The Fermi level lies closer to the conduction band, compared to intrinsic silicon. The P-type on the other hand is doped with an element that has less electrons than silicon. This element is often boron and brings the Fermi level closer to the valence band. Boron, which has one electron less than silicon, contributes a hole, making the P-type a membrane for holes. The N- and P-type work as electron and hole membranes due to the dopant elements changing the electron and hole conductivity respectively in each material [6, p.130].
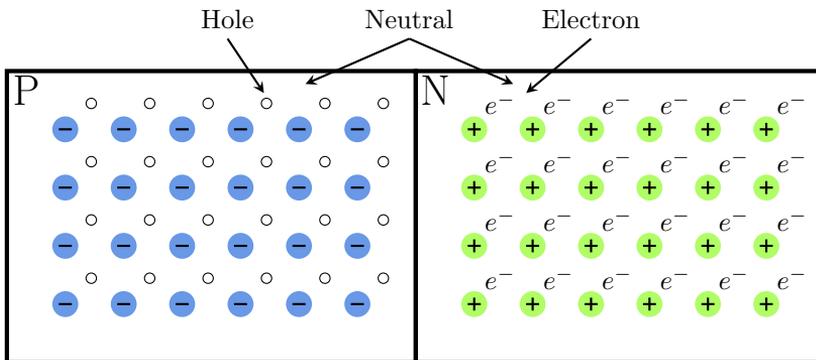

Figure 2.1: A PN-junction before diffusion of mobile charge carriers and creation of the depletion region. Donor atoms (green) and electrons on the N-side, acceptor atoms (blue), and holes on the P-side.

When the PN-junction interface forms, the majority charge carriers will diffuse to the other side due to the concentration gradient over the material. Electrons and holes recombine and charged regions on each side of the junction are formed. This is called the depletion region. Due to the charged regions, an electric field $\boldsymbol{E}$ is present which opposes the concentration gradient and stops further diffusion of majority carriers. Fig. 2.3 shows how the electric field separates an electron-

hole pair that is generated in the depletion region. An electron-hole pair can be separated as long it is generated in the depletion region or within the diffusion lengths of electrons and holes, L_e and L_h respectively.

The formation of the PN-junction will bend the energy bands of the N- and P-type semiconductors due to the charged regions. This results in a gradient in the electrochemical potential of the electrons and holes, which is behind the driving force in a solar cell [6, p.111-113,151-155]. A band diagram of a PN-junction is shown in Fig. 2.2.
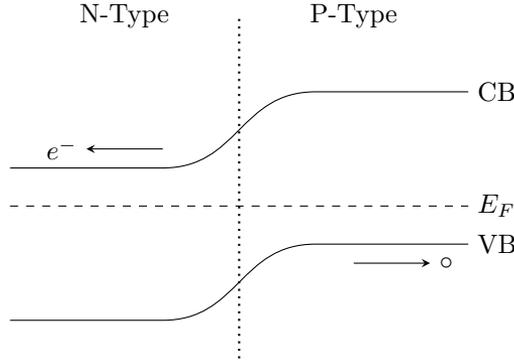

Figure 2.2: Schematic of the bending of the valence and conduction band due to the charged regions in the depletion region. The Fermi level E_F is constant when no light shines on the PN-junction. The N- and P-Type semiconductor acts as membranes for electrons and holes respectively. Thus electrons flows to the left and holes to the right.

The current-voltage characteristic of the PN-junction is expressed as

$$j_Q = j_S \left[\exp \left(\frac{eV}{k_B T} \right) - 1 \right] - e \int_{-L_h}^{L_e} \Delta G_e \, \mathrm{d}x, \tag{2.1}$$

where V is the voltage, T is the temperature, j_S is the reverse saturation current, G_e is the generation of electrons from illumination and k_B is the Boltzmann constant. The voltage over the open terminal in Fig. 2.3, called open circuit voltage is given by Eq. (2.2).

$$V_{oc} = \frac{k_B T}{e} \ln \left(1 - \frac{I_{sc}}{j_S} \right), \tag{2.2}$$

where I_{sc} is the short circuit current expressed as

$$I_{sc} = -e \int_{-L_h}^{L_e} \Delta G_e \, \mathrm{d}x. \tag{2.3}$$
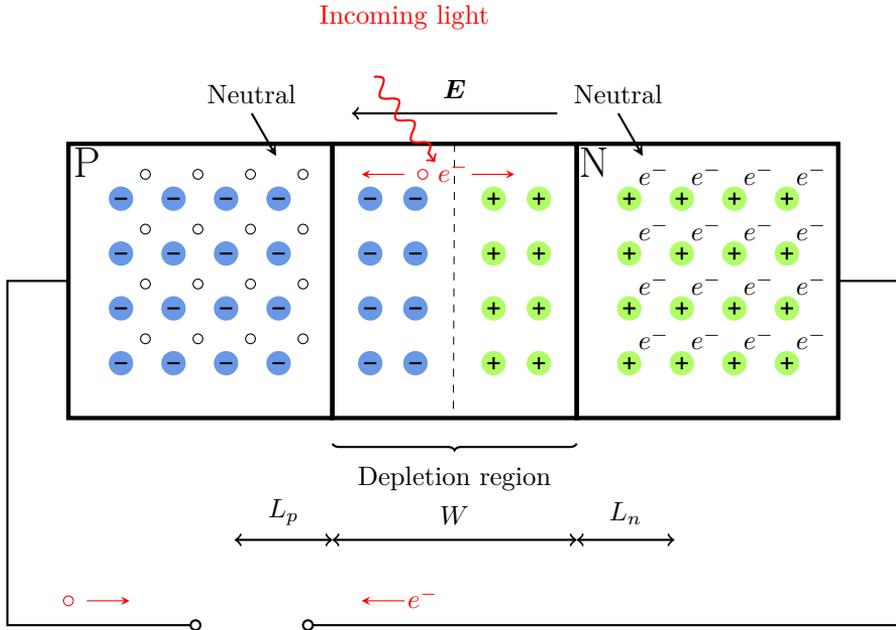
Figure 2.3: PN-junction after diffusion of mobile charge carriers and creation of depletion region of length W, electron and hole diffusion lengths L_n, L_p. Incoming sunlight creates an electron-hole pair which produces a current in the circuit. The electron-hole pair can be separated as long as it is created within W, L_p or L_n.

Since solar cells can be very different from one another, the efficiency η is used for comparison. To find the efficiency of a solar cell one must first find the maximum power output P_m. By maximizing an area under the current-voltage curve, in this case for a typical solar cell as shown in Fig. 2.4, P_m can be found. The maximum current and voltage I_m and V_m gives the maximum power output via the simple relation

$$P_m = I_m V_m. \tag{2.4}$$

The efficiency is the fraction of power output of the total power incident P_{inc} from the sun onto the solar cell. It is expressed as

$$\eta = \frac{P_m}{P_{inc}} = \text{FF} \cdot \frac{I_{sc} V_{oc}}{P_{inc}}. \tag{2.5}$$

Here the fill factor $\text{FF} = P_m / I_{sc} V_{oc}$ is introduced, another important figure for comparing solar cells. The fill factor gives the ratio of the maximum obtainable power to the product of the open circuit voltage and short circuit current.
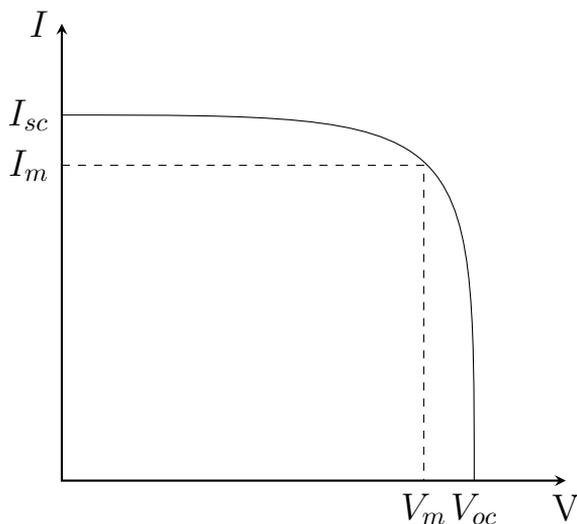
Figure 2.4: The current-voltage characteristic of a solar cell. The current I_m and voltage V_m maximize the area under the IV-curve. This point gives the maximum power output P_m and the greatest efficiency of the solar cell.

2.1.2 Limitations on Efficiency

Even though the theoretical efficiency of solar cells can be quite high, the real situation is a bit different. Solar cells are far from achieving their theoretical potential due to many factors. These factors can take many forms, and in order to produce the best solar cells, it is vital to understand what they are in order to prevent decreases in efficiency as much as possible. Some factors can be overcome by producing better cells, while some are governed by physical laws and cannot be helped.

Quantum Efficiency

Quantum efficiency is a measure of how well a solar cell makes use of the incident solar spectrum. More specifically it gives the number of electrons excited in the solar cell per incident photon. This quantity is called the external quantum efficiency (EQE). Another quantity, called the internal quantum efficiency (IQE), accounts for reflection and transmission through the solar cell. It is expressed as

$$IQE = \frac{EQE}{1 - R - T},$$

(2.6)

where R and T are coefficients for reflection and transmission respectively. If a material reflects a lot of the incoming radiation, the efficiency will suffer. Some counter measures used on commercial cells are anti reflective coating (ARC) and

of the surface. Both measures ensures more photons being used to generate electrical energy, thus increasing the overall efficiency of the solar cell.

Recombination

Some electron-hole pairs will recombine, which is the reverse reaction of electron-hole pair generation. This is a very significant contribution to the efficiency decrease of a solar cell. The energy can be dissipated as a photon, phonon or both. There are two kinds of recombination, radiative and non-radiative.

Radiative recombination is the exact reverse process of electron-hole generation. An electron in the conduction band can spontaneously fill an empty state in the valence band. The result is the emission of a photon. However, the emitted photon does not necessarily correspond to a loss. The emitted photon can excite another electron, generating a new electron-hole pair. It is only counted as a loss if it escapes the solar cell material. Since radiative recombination is a spontaneous process, the effect cannot be completely prevented, only minimized by making sure that the solar cell is thick enough to make reexcitation probable.

Non-radiative recombinations do not release energy as a photon. Instead, the energy is released via other electrons and holes, called Auger recombination, or through phonons, called impurity recombinations. Auger recombination is the reverse process of impact ionization. The energy released through recombination is transferred to an electron or hole that proceeds to lose that energy to the lattice through phonon collisions. The process is practically unavoidable and determines the efficiency limits of the best silicon solar cells. This is due to the relation between Auger recombination and doping levels [6, p.78].

Impurity recombinations are perhaps the most important recombination type. Impurities can introduce available states in the otherwise forbidden bandgap. This hinders generation of electron-hole pairs that can be extracted into the circuit. The statistics of this mechanism have been studied and explained in detail by Shockley, Read and Hall in 1952 [7, 8] and is the reason why impurity recombination is often called Shockley-Read-Hall-recombination (SRH-recombination). However, the physical mechanism is not straight forward to understand. The most widely accepted theory is lattice relaxation multiphonon emission (MPE), explained by Lang and Henry in 1975 [9]. Similar to impurities, grain boundaries and surfaces also work as recombination centers.

2.1.3 Intermediate Band Solar Cells

Intermediate band solar cells are one of the more promising third generation solar cell concepts. An IBSC is based on a material where a rather narrow, intermediate energy band is present within the bandgap of the semiconductor it is made of. This extra band allows better utilization of both low and high energy

photons, as illustrated in Fig. 2.5. Additionally, there is only one extra layer of material needed compared to conventional solar cells, which means that the extra cost is low. The theoretical efficiency limit for such solar cells is 63.1%, much higher than the 40.7% of the first and second generation cells under the same operating conditions [4, 10].
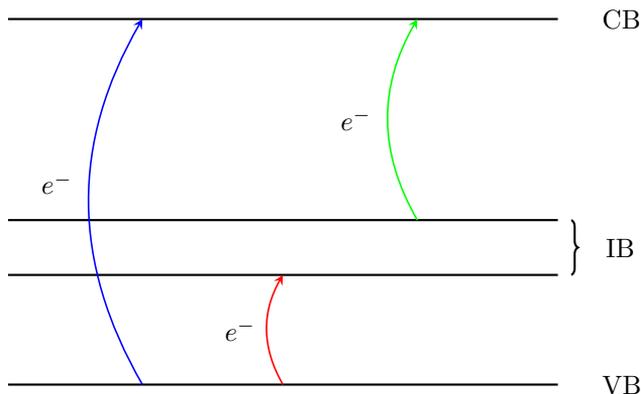

Figure 2.5: Schematic showing how an intermediate band of states in the bandgap can utilize more of the solar spectrum. Electrons can be excited from the valence band (VB) to the intermediate band (IB) by low energy photons (red) and from the IB to the conduction band (CB) by photons with intermediate energy (green). Above bandgap energy photons (blue) can excite electrons directly from the VB to the CB like in a traditional solar cell.

The concept is to sandwich the intermediate band (IB) between a P- and N-type semiconductor as illustrated in Fig. 2.6. Photons with energy lower than the bandgap, are unable to generate electron-hole pairs in a conventional cell. In an IBSC however, lower energy photons can excite electrons from the VB to the IB or from the IB to CB, while photons with energy greater than the bandgap can excite electrons directly from VB to CB. The current is extracted through the P- and N-type materials as usual. This means that the voltage over the cell is not reduced by the IB material. Using a IB material with a large bandgap, can even increase the voltage, although it is a trad-off since little sunlight can excite from the VB to the CB if the bandgap is too large. This makes use of sub bandgap photons, thus more solar energy is converted to electrical energy. An ideal IBSC has a bandgap of 1.95 eV which is split by the IB into sub bandgaps of 0.71 eV and 1.24 eV [10]. As long as the photon energy is greater than 0.71 eV, the photon can be absorbed.

There are three proposed designs of realizing the IBSC concept [10]. The three designs are: utilizing confinement effects in quantum dots, fabrication of highly mismatched alloys and ultrahigh doping (UHD-IBSC). The quantum dot ap-
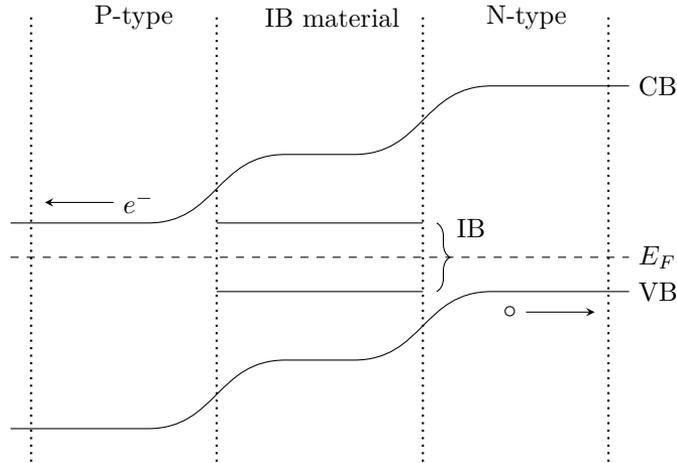
Figure 2.6: Schematic of the valence and conduction bands of a P-IB-N device. Electron-hole pairs generated in either of the three regions have the possibility of getting collected. The P- and N-type only allows above band gap photons, while the IB material can absorb sub band gap photons as in Fig. 2.5. The P- and N-type semiconductors work as electron and hole membranes.

proach is currently the most developed approach, with the best cells reaching an efficiency of 18.7% [11] under AM1.5G 1 sun conditions. A common problem with all the designs are that scarce or toxic elements are often used. An exception to this, and a candidate for UHD-IBSCs, is chromium doped zinc sulfide (ZnS:Cr). Here the idea is to have Cr form energy levels inside the bandgap of ZnS. The idea might seem counter intuitive at first since impurities are a source of non-radiative recombinations. Still, experimental evidence show that Si samples heavily doped with Ti gives less SRH-recombinations than samples with less Ti. The reason to this is rather complex and is explained by Luque and Martí [12]. ZnS is covered in greater detail in section 2.3.

2.2 Transmission Electron Microscopy

On our quest to discover the properties of materials and invent new devices, microscopy techniques are essential. There is a strong correlation between the structure of a material and its properties. Powerful microscopes are needed to study these structures at the nano scale. Visible light microscopes (VLM) can not see these fine details. This motivated the development of a new breed of microscopes using electrons instead of light. The first commercial transmission electron microscope (TEM) was built in the UK in 1936, only 4 years after the term was first used in a paper by Ernst Ruska and Max Knoll [13, p.4].

2.2.1 The Instrument

The most obvious difference between a TEM and a VLM is that a TEM uses electrons to "see", rather than photons. In a VLM photons are reflected from the specimen surface into a the magnifying system of the microscope in order to get an image. In a TEM a beam of electrons are sent at high speed through an electron transparent specimen. The electrons interact with the specimen material and are transmitted and detected. The transmitted electrons form an image that is a two-dimensional projection of the three-dimensional specimen.

Generally a TEM consists of three parts stacked vertically in a column. These are the illumination system consisting of an electron gun and condenser lenses, an objective lens and specimen stage, and an imaging system. Depending on the TEM this list can be a lot longer as it can be equipped with a variety of sensors and detectors for different tasks. There are two main modes in which a TEM is operated. The difference lies in whether the beam of electrons is focused before the specimen or not. The basic imaging and diffraction mode uses a parallel beam, while more advanced techniques like scanning transmission microscopy (STEM) imaging and analysis via X-ray and electron spectrometry use a convergent beam. Fig. 2.7 shows how electrons go through a TEM column in the parallel beam mode and is comparable to a ray diagram for an optical system.

2.2.2 Resolution

The Rayleigh criterion [13, p.5] states the smallest resolvable distance, δ, for a VLM,

$$\delta = \frac{0.61\lambda}{\mu \sin \beta}.$$

(2.7)

Where λ is the wavelength of light, μ is the refractive index of the viewing medium and β is the collection semi-angle of the magnifying lens. If the VLM is in vacuum and has the largest possible collection angle, the resolution limit will be $335 \, \text{nm}$ using green light at a wavelength of $550 \, \text{nm}$, which is over 600 times the length of the unit cell in silicon. To study features at the atomic scale the information carriers need to have a smaller wavelength.

In 1925 Louis de Broglie postulated that electrons have both particle and wave properties. This wave-particle duality is known as the de Broglie hypothesis, and for this discovery de Broglie was awarded the Nobel Prize in Physics in 1929. The wavelength of an electron is expressed in terms of Planck's constant, h and momentum, p.

$$\lambda = \frac{h}{p}.$$

(2.8)

The classical momentum $p = m_e v$, where m_e is the electron mass and v is the velocity, does not hold true for electrons at relativistic speeds. The relativistic
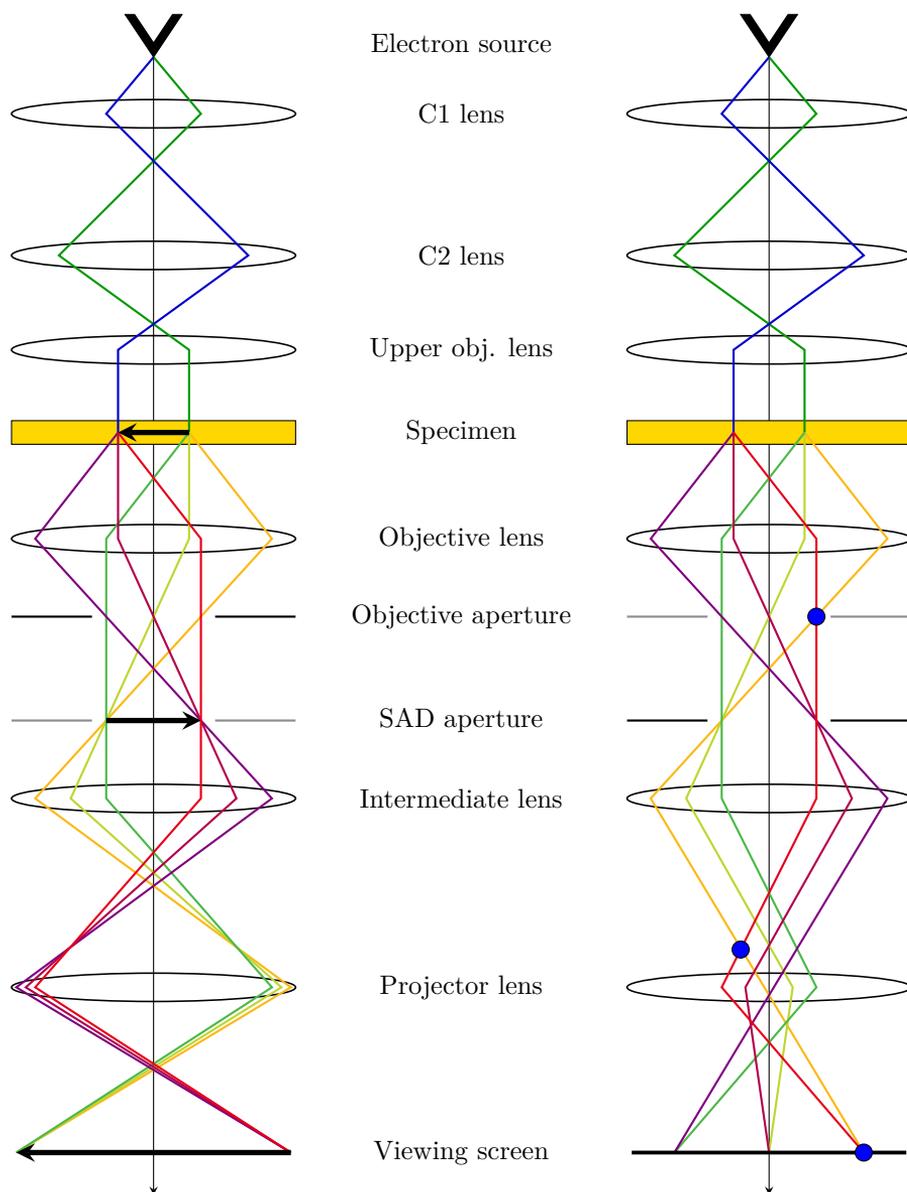
Figure 2.7: A simplified sketch of a TEM operating in the image mode (left) and in the diffraction mode (right). In the imaging mode the image plane located at the retracted SAD aperture is magnified and projected onto the viewing screen. In the diffraction mode it is the back focal plane at the objective aperture. Note that real TEMs have many more lenses than what is shown here. Figure inspired by Fig. 9.1 and 9.12 in [13, p.142,152].

formula relating kinetic energy, E_k, to momentum is

$$E_k = \sqrt{p^2c^2 + m_e^2c^4} - m_ec^2 \tag{2.9}$$

or

$$p = \left(2m_eE_k\left(1 + \frac{E_k}{2m_ec^2}\right)\right)^{1/2}. \tag{2.10}$$

By inserting (2.10) into (2.8), the wavelength of an electron is found to be

$$\lambda = \frac{h}{\left(2m_eE_k\left(1 + \frac{E_k}{2m_ec^2}\right)\right)^{1/2}}. \tag{2.11}$$

This means in the case of a typical TEM, where the electrons are accelerated over a potential of $200\,\text{kV}$, the wavelength is $\approx 1.8\,\text{pm}$. By (2.7) the theoretical resolution limit is $\approx 1\,\text{pm}$. This is much smaller than the diameter of an atom, which is typically around $1\,\text{Å}$. Unfortunately this resolution limit is out of reach. This is mainly due to spherical aberrations in the electromagnetic lenses used in TEMs. Still, TEMs have come a long way since the efforts of Ruska and Knoll. State of the art TEMs with aberration-correction can resolve details less than $1\,\text{Å}$ apart, making it possible to resolve atoms.

2.2.3 Signals in TEM

The electron beam is ionizing, meaning that it has enough energy to eject the innermost electrons of the atoms it interacts with. This is one of the reasons why the TEM is such a versatile instrument. The ionizing radiation generates a wide range of signals, which is summarized in Fig. 2.8. The most important are also explained below.

Elastic electrons are electrons that do not lose energy on their way through the specimen. Elastic electrons interact with the specimen through the Coulomb force. This Coulomb interaction can either be with the negatively charged electron cloud or the positively charged nucleus of the atoms in the specimen. Interactions with the electron cloud scatter the electron beam to relatively low angles. [13, p.41] Scattering to higher angles is due to interactions with the nucleus. The elastic electrons, found in the direct beam and the diffracted beams, are used for TEM imaging and diffraction.

Inelastic electrons are electrons that lose some energy on their way through the specimen. The lost energy produces a new signal, which can be characteristic X-rays, bremsstrahlung X-rays, secondary electrons, Auger electrons, plasmons or phonons. The inelastic electrons are mostly forward scattered, and are studied with energy electron loss spectroscopy (EELS).

Characteristic X-rays are created when an electron is returning to a lower energy state. Incoming electrons can transfer a critical amount of energy to a
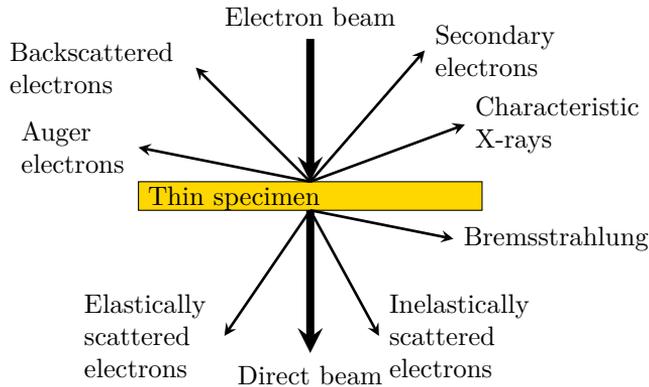
Figure 2.8: Schematic showing the variety of signals generated when the electron beam interacts with the specimen. The direction of the arrows does not accurately show the direction of the signal, instead it gives an idea of where the signal is strongest. Figure inspired by Fig. 1.3 in [13, p.7].

K shell electron which excites it above the Fermi energy level [13, p.55]. The empty K shell energy state can be occupied by an electron from a higher energy state. The process of changing energy state from high to low yields a photon with energy equal to the energy difference between the initial and the final state. These photons are called characteristic X-rays because different elements have different energies between states. Energy dispersive X-ray spectroscopy (EDX) is an elemental analysis technique that makes use of the characteristic X-rays.

Contrast Mechanisms

TEM images are in grayscale. The more intensity a pixel on the detector gets, the whiter it will appear. Understanding the contrast mechanisms is vital to interpret TEM images. There are two types of contrast, amplitude and phase contrast. An effective TEM user needs knowledge about both of them [14].

Amplitude contrast is often divided into mass-thickness contrast and diffraction contrast. Mass-thickness contrast is due to specimen thickness and the mass of the atoms in the specimen. A thicker sample will be less transparent to electrons, thus fewer electrons will be transmitted, giving a weaker signal. The atomic scattering factor, $f(\theta)$, relates the amplitude of a scattered electron wave to the atomic number Z. The atomic scattering factor is defined as

$$f(\theta) = \frac{\left(1 + \frac{E_{beam}}{m_e c^2}\right)}{8\pi^2 a_0} \left(\frac{\lambda}{\sin \theta/2}\right)^2 (Z - f_x),$$ (2.12)

where a_0 is the Bohr radius and f_x is the scattering factor for X-rays. The absolute squared value $|f(\theta)|^2$ is proportional to the scattered intensity [13, p.44].

It is then clear from the equation that more massive atoms scatter electron waves more than less massive atoms.

Diffraction contrast is the main source of contrast in bright field and dark field TEM. Simply put, the scattering of the electron beam is dependent on the crystal orientation. This means that crystal grains oriented in different directions, scatter the electron beam differently. As a consequence of this, some grains will appear dark while others appear brighter in a polycrystalline specimen. Diffraction is explained in greater detail in section 2.2.4.

Phase contrast is often synonymous with high resolution TEM (HRTEM). In HRTEM the objective aperture is removed and several diffracted beams contribute to the formation of the image. The effects of phase contrast are seen as fringes. The fringe patterns can be caused by thickness variations, stacking faults or be Moiré patterns. A Moiré pattern is created by two or more crystal grains laying on top of each other in different orientations. It is the interference of two periodic structures.

2.2.4 Techniques in TEM

Due to all the available signals and different contrast mechanisms, there are a lot of information to be extracted from a specimen in TEM. Most TEMs are equipped with many detectors to record the different signals. This section will explain some of the most common TEM techniques and the physical principles behind them.

Diffraction

Diffraction in TEM is an interference phenomenon analogous to diffraction of electromagnetic radiation in Young's double slit experiment [15, p.169]. In TEM the electron wave is the electromagnetic radiation and the crystal structure of the specimen acts as the slits. More specifically the "slits" in the crystal is the distance between planes of atoms, which are described by the Miller indices [16, p.11]. The theory behind diffraction was developed for X-rays but is also applicable for electrons when treated as waves. Diffraction of crystals by X-rays was discovered by Max von Laue. He found that diffraction only happen under very specific conditions. Laue was awarded the Nobel Prize in Physics for this discovery in 1914.

First, recall that the reciprocal lattice is the Fourier transform of the real crystal lattice and that the real lattice vector, $\boldsymbol{R}$, is perpendicular to the reciprocal lattice vector, $\boldsymbol{G}$. The Laue condition assumes that the electron waves are scattered elastically. The incident and scattered electron waves are described by wave vectors, $\boldsymbol{k}$ and $\boldsymbol{k'}$ respectively. More specifically

$$\boldsymbol{k} = \frac{2\pi}{\lambda}\hat{n}. \tag{2.13}$$

and

$$\boldsymbol{k}' = \frac{2\pi}{\lambda}\hat{n}. \tag{2.14}$$

Since diffraction is an interference phenomenon, the incoming electron waves must scatter in phase with each other. Consider Fig. 2.9 where $\boldsymbol{k_1}$ travels a bit further than $\boldsymbol{k_2}$ before the scattering event. Interference will only happen if the extra distance traveled by $\boldsymbol{k_1}$ is an integer multiple of the wavelength of the electron wave,

$$\boldsymbol{d} \cdot \hat{n} + -\boldsymbol{d} \cdot \hat{n}' = \boldsymbol{d} \cdot (\hat{n} - \hat{n}') = m\lambda, \tag{2.15}$$

where m is an integer. Eq. (2.15) can be expressed in terms of wave vectors by multiplying with $2\pi/\lambda$,

$$\boldsymbol{d} \cdot (\boldsymbol{k} - \boldsymbol{k}') = 2\pi m. \tag{2.16}$$

The following manipulation yields the Laue condition

$$e^{i(\boldsymbol{d} \cdot (\boldsymbol{k} - \boldsymbol{k}'))} = 1 \tag{2.17}$$

which only hold true if the scattering vector $\boldsymbol{k} - \boldsymbol{k}'$ is a reciprocal lattice vector $\boldsymbol{G}$. The Laue condition can also be pictured by considering Eq. (2.18),
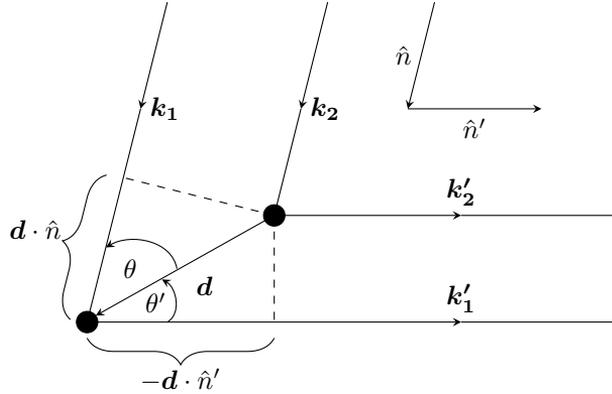
Figure 2.9: Ray diagram of two incoming electron waves, $\boldsymbol{k_1}$ and $\boldsymbol{k_2}$, scatter on a crystal plane with lattice vector $\boldsymbol{d}$. Diffraction will only occur if the two waves scatter in phase. The extra distance $\boldsymbol{k_1}$ must travel has to be an integer multiple of λ.

$$\boldsymbol{G} = \boldsymbol{k}' - \boldsymbol{k}. \tag{2.18}$$

Squaring both sides yields

$$k^2 = k^2 + G^2 - 2k \cdot G \tag{2.19}$$

where $|\boldsymbol{k}'| = |\boldsymbol{k}|$ since elastic scattering is assumed. Eq. (2.19) can be written as

$$\frac{G}{2} = \boldsymbol{k}\frac{\boldsymbol{G}}{G} = \boldsymbol{k} \cdot \hat{G}. \tag{2.20}$$

which means that the length of $\boldsymbol{k}$ along $\boldsymbol{G}$ has to be half as long as $\boldsymbol{G}$. This restricts $\boldsymbol{k}$ to have its tip in a perpendicular plane bisecting $\boldsymbol{G}$ for diffraction to occur. These planes perpendicular to $\boldsymbol{G}$ are called Bragg planes, named after William Lawrence Bragg who formulated a simple equation relating scattering angle θ with lattice plane spacing d known as the Bragg law [16, p.25]. Assuming specular reflection of the electron waves, the extra distance $\boldsymbol{k_1}$ has to travel in Fig. 2.9 is now $2d\sin\theta$, which gives

$$2d\sin\theta = m\lambda. \qquad (2.21)$$

Paul Peter Ewald developed a geometrical construct to make it easier to visualize which (hkl) planes will give diffraction. This construction is called the Ewald sphere. Fig. 2.10 is showing an Ewald sphere in 2 dimensions, but a real Ewald sphere exists in a 3 dimensional reciprocal space. The Ewald sphere is constructed by first drawing the incident wave vector $\boldsymbol{k}$ so that its tip points at a reciprocal lattice point. A circle of radius $\boldsymbol{k} = 2\pi/\lambda$ is drawn with about the origin of $\boldsymbol{k}$. Any point in the reciprocal lattice intersected by the circle will fulfill the Laue condition, $\boldsymbol{k} - \boldsymbol{k}' = \boldsymbol{G}$. This means that the set of (hkl) planes associated to that point will be visible in a recorded diffraction image.
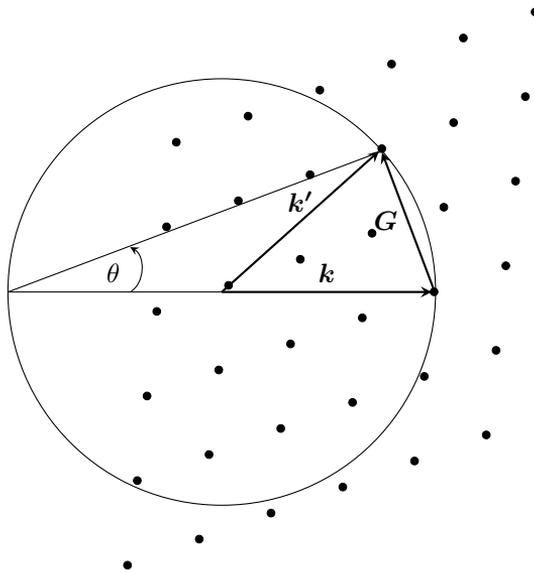
Figure 2.10: The Ewald "sphere" in a 2 dimensional reciprocal lattice. The Ewald sphere is constructed so that the tip of $\boldsymbol{k}$ lies in a reciprocal lattice point with a circle of radius $|\boldsymbol{k}| = 2\pi/\lambda$ about the origin of $\boldsymbol{k}$. Any lattice point intersecting the circle will form a diffracted beam with the Bragg angle, θ in Eq. (2.21).

Diffraction in TEM works by adjusting the lenses so that the back focal plane

is imaged on the TEM viewing screen or CCD detector as in Fig. 2.7. Beams reflected to the same angle originates from a common set of (hkl) planes. Since the wavelength is so small in TEM, the Ewald sphere becomes very large because of the inverse relationship $\boldsymbol{k} = 2\pi/\lambda$. The bigger the Ewald sphere, the more reciprocal lattice points it will intersect. This is why a TEM diffraction pattern contains so many reflections. However, diffraction images are dependent of a number variables.

Since diffraction patterns are images of real space crystal planes fulfilling the Laue condition, they depend on the crystal structure of a material. Plane to plane distance d_{hkl} varies among the crystal structures, so two crystal structures give different diffraction images. The direction of the (hkl) planes also matters. This is well illustrated by comparing a diffraction image of a single crystal and a polycrystal. The single crystalline Si in Fig. 2.11(a) show strong pointlike reflections (indexed), while the the polycrystalline ZnS in both images produce circles. Assuming single scattering through a crystal, reflections that will be

(a)   (b)
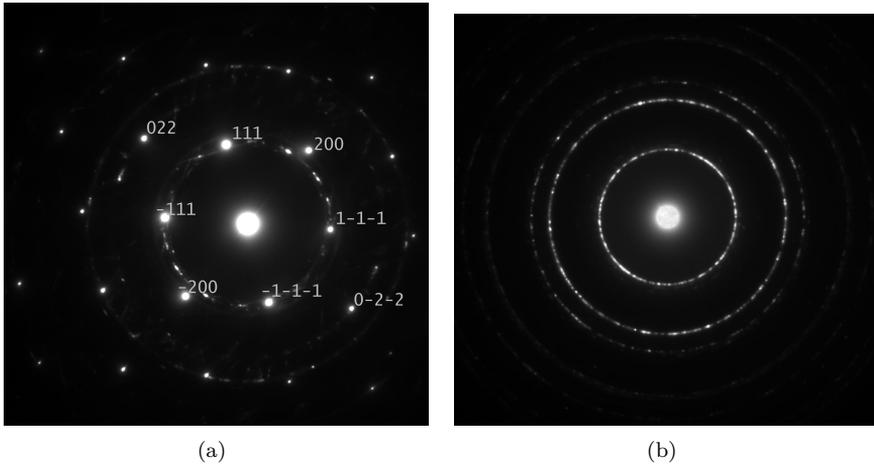
Figure 2.11: a) Diffraction image of the cross section of a polycrystalline ZnS thin film on top of a single crystalline Si substrate. **b)** Diffraction image of polycrystalline ZnS in plan view. The number of grains make a big difference in how pronounced the ring pattern is.

present in a diffraction image is expressed by the structure factor,

$$F_{hkl} = \sum_{j=1}^{n} f_j \exp 2\pi i \left(\frac{hx}{a} + \frac{ky}{b} + \frac{lz}{c} \right). \qquad (2.22)$$

The equation is a sum over all the atoms j in the unit cell, f_j is the atomic scattering factor for atom j and a, b and c are the lattice parameters. The structure factor shows that not all (hkl) reflections will give diffraction, some

are extinct. An example is the (200) reflection in a face centered cubic material such as Si. However, in TEM diffraction images the (200) reflection in Si is not extinct. This is due to the strong interaction between the incoming electrons and the material not fulfilling the single scattering assumption.

Notice how the reflections are not sharp points like one might assume from the theory above. The reflections stretch out a bit, looking more like dots than points. This is due to the electron beam not being perfectly collimated and because the lattice is expanding and contracting with temperature variations.

Diffraction images are also dependent on how the crystal is oriented with respect to the electron beam. The term zone axis is used to denote this orientation, and is expressed with Miller indices in a square bracket [hkl]. A zone axis [hkl] is perpendicular to the (hkl) plane.

Bright and Dark Field TEM

Bright field (BF) and dark field (DF) are two imaging techniques where the diffraction pattern is used to select which reflections should contribute to the final image. The selection is done with the objective aperture. In BF the direct beam is selected. This gives an image formed by unscattered electrons. Crystal grains that diffracts the beam appear darker than grains that do not fulfill the Laue condition. Parts of the beam passing through vacuum will appear very bright, which is why it is called bright field.

In DF, a single scattered reflection is chosen by the use of a selected area aperture to make an image. This way, only a specific set of (hkl) planes is imaged. Since no unscattered electrons are imaged, vacuum will look black, hence the name dark field.

Scanning Transmission Electron Microscopy

Scanning transmission electron microscopy (STEM) is a powerful tool for both imaging and spectroscopy. TEM and STEM are commonly differentiated due to the difference in the working principle. Where the TEM mode illuminates the whole specimen before focusing the transmitted electrons through a lens system, the STEM mode scans a fine electron probe across the area of interest. The transmitted beam in each point is collected by a dedicated BF or DF STEM detector to form images.

In order to acquire an image of contrast comparable to one captured in TEM mode, the electron probe must be parallel to the optical axis at all times. If the electron probe was pivoting about a point above the specimen like in a scanning electron microscope (SEM) , the contrast in images aquired in STEM would be very difficult to understand. Double deflection scanning coils in addition to the usual lenses above the specimen ensures a fine probe that is parallel to the optical

axis in each point in the scan. When combined with spectroscopy techniques, STEM can give elemental and chemical data from very small areas. A skilled user can obtain a lot of specimen information out of the large data set generated.

BF and DF STEM detectors are geometrically a bit different from the ones used in the TEM mode. The BF detector is a point detector that sits in a plane conjugate to the back focal plane where the diffraction pattern is formed. It collects electrons originating from the direct beam and maps the intensity in each point of the scan to a pixel in the image.

DF STEM is different from DF TEM in how images are detected and what information they give. Unlike in TEM mode, a selected area aperture is not used for DF STEM. Instead of choosing single reflections to image, DF STEM is an image of all electrons scattered between two angles specified by the distance from the sample to the diffraction pattern in the back focal plane. Since the DF STEM detector is an annulus, this is possible. The distance from the sample to the diffraction pattern is called the camera length L. A shorter camera length means electrons scattered to higher angles are collected and vice versa. Fig. 2.12 shows a schematic of the detector setup.

DF STEM detectors are divided into two categories, high angle and low angle annular DF, abbreviated HAADF and LAADF respectively. In HAADF the dominating source of contrast is from high angle elastic scattering events. This type of amplitude contrast is called Z-contrast due to more massive elements scatter more to higher angles than less massive elements, which is understood from Eq. 2.12. It is important to use a sufficiently small enough L to ensure that Z-contrast really is dominating over diffraction contrast. If a too large camera length is chosen, both diffraction and Z-contrast are present and it is easy to draw the wrong conclusion.

Energy-Dispersive X-ray Spectroscopy

Energy-dispersive X-ray spectroscopy (EDX) is a chemical characterization technique utilizing the characteristic X-rays produced by the electron beam.

Characteristic X-rays are created when an electron is returning to a lower energy state. This can happen when an incoming electron has transferred a critical amount of energy to a K shell electron, thus exciting it above the Fermi energy level. The empty K shell energy state that remains can be occupied by a an electron in a higher energy state for instance from a K or M shell energy state. In this process the electron has to give off some of its energy. This energy is given off as a photon and is equal to the energy difference between the initial and the final state. The X-rays are given names depending on these states and usually called X-ray lines. The set of possible energy differences gives each element its own fingerprint, and the energy released corresponds to a photon in the X-ray regime, hence the name characteristic X-rays.

Electron probe
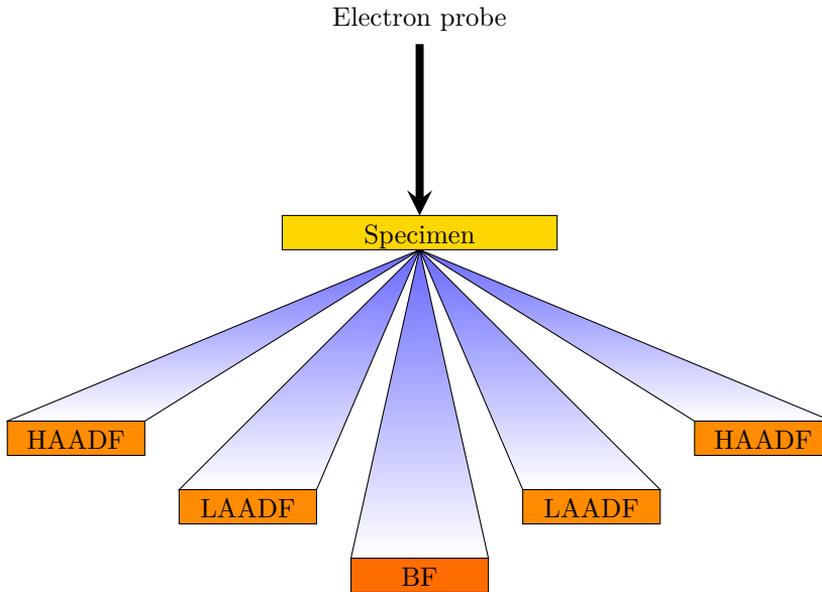
Figure 2.12: Cross sectional schematic illustrating the detector setup in STEM. The BF detector sits in a plane conjugate to the back focal plane in order to collect the direct beam. The LAADF and HAADF detectors are annular detector that are collecting electrons scattered in an angular range specified by the camera length. Figure inspired by Fig. 9.19 in [13, p.160].

The most important parameter to consider when acquiring an EDX spectrum is the number of X-rays per second often called number of counts. To get the best statistics, and thus the best basis to say something about the specimen, a sufficient number of counts are needed. The number of counts are affected by many factors. The thickness of the specimen, absorption and fluorescence all affect the number of counts [17, p.597]. An X-ray created inside the specimen must travel through the rest of the material and get to the detector. While inside the specimen it can be absorbed, or partially absorbed and leave a fluorescent X-ray and bremsstrahlung. The thickness and the tilt of the specimen influences absorption and fluorescence measured. The longer an X-ray travels through a material increases the chance of absorption or inelastic collisions. On the other hand, a too thin specimen may not produce a sufficient number of counts as it is possible for electrons to pass straight through the specimen with no collision.

The raw EDX data on its own is not enough to make quantitative conclusions. Elements have different probabilities of producing characteristic X-rays, the mean free path and flourescence of X-rays vary at different positions in the specimen. To account for this, the Cliff-Lorimer ratio technique can be applied [17, p.640]

$$\frac{C_A}{C_B} = k_{\text{AB}} \frac{I_A}{I_B}.$$ (2.23)

The Cliff-Lorimer ratio relates the ratio of element A and B, C_A and C_B respectively, to the measured intensity of element A and B, I_A and I_B respectively, through a sensity factor k_{AB}. The sensitivity factor k_{AB} must be measured with a standard specimen where the ratio of element A and B is known, then it can be applied to the EDX spectra of other specimen.

Electron Energy Loss Spectroscopy

Electron energy loss spectroscopy (EELS) is a technique using forward scattered elastic electrons and inelastic scattered electrons. EELS gives the number of electrons as a function of the energy loss through the specimen and can be used for a variety of tasks. Analysis of the EELS data can yield information about sample thickness, dielectric constant, chemical shift and valence state of elements.

The selection of forward scattered elastic electrons and inelastic scattered electrons are done by an entrance aperture at the optic axis. Bragg scattered electrons will hit the aperture and will not contribute to the signal. The electrons are then traveling through a magnetic drift tube that deflects the signal 90° away from the optical axis. In order to measure the number of electrons as a function of the energy loss, a magnetic prism is used to separate electrons of different energy. The Lorentz force will deflect lower energy electrons more, i.e. electrons that have lost more energy. After being deflected, a multipole projector lens system ensures that the electrons are well separated spatially as a function of their energy, and that electrons with the same energy strike the detector at the same place. A schematic of how electrons move through an EELS setup is illustrated in Fig. 2.13.

The EELS spectrum is divided into two parts, one covering the low loss electrons and the other the high loss electrons. Each part of the spectrum gives useful information about specimen, and are often used in conjunction. The primary features of the EELS spectrum and the information contained is explained below.

The low loss spectrum is defined to cover a range from $0\,\mathrm{eV}$ to $50\,\mathrm{eV}$. The range has two important features, the zero loss peak and the plasmon peaks. The zero loss peak represents the electrons transmitted through the specimen without losing energy. Ideally, the zero loss peak should be a thin line, but is broadened due to the electron beam not being completely monochromatic. An electron source will always have a slight spread in energy that broadens every feature in both low and high loss spectra. Because of this, the zero loss peak at full width at half maxmium (FWHM) gives the energy resolution of the spectrum. A much weaker and broader peak is apparent next to the zero loss peak. This is due to the creation of plasmons which are quantized plasma oscillations, much like phonons are quantized lattice vibrations. The plasmon peak arises due to electron-electron interactions between the incident electron beam and weakly bound electrons in the conductance or valence band. If the sample is thick enough, higher orders of
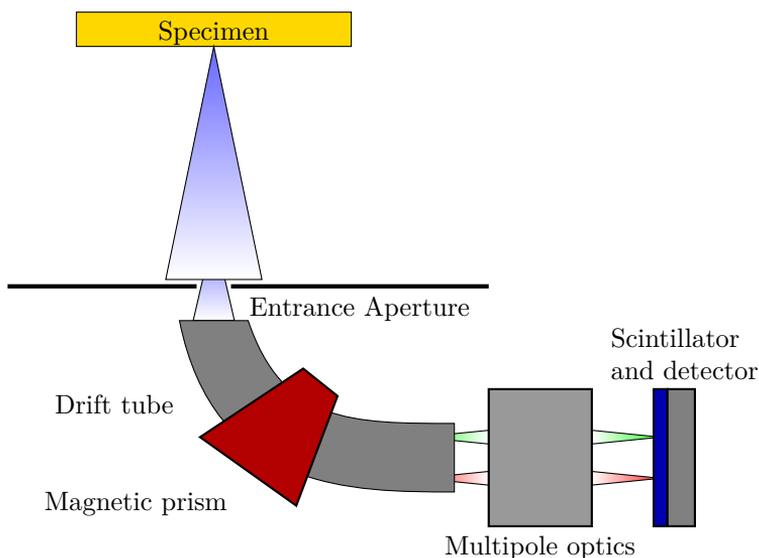
Figure 2.13: Schematic illustrating the key parts in an EELS setup in TEM. Forward scattered elastic and inelastic electrons are selected by an entrance aperture. The selected electrons travels through a drift tube which deflects them away from the optical axis while being separated in energy by a magnetic prism. A scintillator and detector counts the number of electrons of each energy.

the plasmon peak is seen behind the first one and also every other feature in the high loss spectrum will have trailing plasmon peaks.

The high loss spectrum covers electron losses in a user defined range to fit the element to be analyzed. This range contains information about inelastic interactions with inner or core shell electrons. The phenomenon is the same as in EDX, but in this case it is the electron loss that is measured rather than the X-ray emission. There are some differences separating EELS from EDX. The nature of the magnetic prism spectrometer gives EELS much greater energy resolution than EDX at the cost of not being able to measure signals from all elements at once. EELS is not suitable for all elements, heavy elements suffer from the signal exponentially decaying with increasing energy. A feature in the high loss spectrum called an ionization edge, is due to the ionization of an atom. The ionization edges are given names depending on which electron orbital the energy loss is associated with. The high energy resolution of EELS makes it possible to distinguish orbitals from within the same shell. In addition to elemental analysis, it is also possible to determine the valence state of an element.

Valence state determination is done by analyzing the fine structure signal from a given element. Fine structure is an effect of splitting of atomic energy levels due to spin-orbit coupling. The fine structure energy levels are also affected by the valence state of the atom. If the atom is missing or has extra electrons, then

the energy levels of the remaining electrons will shift because of the change in Coulomb forces acting on them. Even though fine structure works as a chemical fingerprint, complications can arise if two elements with similar fine structure are analyzed together.

2.2.5 Disadvantages

While the TEM has many advantages over other microscopy techniques, it also has its drawbacks. One of the most obvious drawbacks is that a modern TEM is very expensive. The price can range from 5 MNOK to 50 MNOK for state of the art machines.

The high resolution of TEM also comes with a drawback. When looking at small details, it becomes very time consuming to study a lot of them. TEM is therefore not the best tool for generating statistics. Because of this and the high cost, makes the TEM not suitable for initial studies of a new material, other instruments like VLM and SEM are used first.

Results from TEM are also very dependent on specimen quality. In order to get the best data, the specimen usually has to be very thin and clean. For instance, a contaminated specimen can yield useless STEM images due to hydrocarbons piling up and covering the area of interest. A sample free from hydrocarbons can be hard to achieve.

TEM is also limited to what materials can be studied due to the strong interaction between electrons and matter. Some materials, mainly biological, are susceptible being damaged by the electron beam. This is called beam damage and will in some cases alter the crystal structure of the specimen. Using a lower acceleration voltage might be an option in some cases, but it is favorable to use the highest acceleration voltages available with respect to resolution.

2.3 Materials

This section will cover some background information about zinc, sulfur and chromium. Some details on the possible crystal structures for ZnS and electronic structures for Cr are explained.

Zinc sulfide is a polymorphic inorganic wide-bandgap semiconductor. Both zinc and sulfur are low-toxicity elements found abundantly in the earth's crust [18]. Zinc and sulphur are number 30 and 16 in the periodic table respectively. Due to its optical and electrical properties, and abundance, ZnS is used in a range of applications and is a so-called functional material. Examples of applications are electroluminescent devices, blue and ultraviolet light emitting diodes, laser
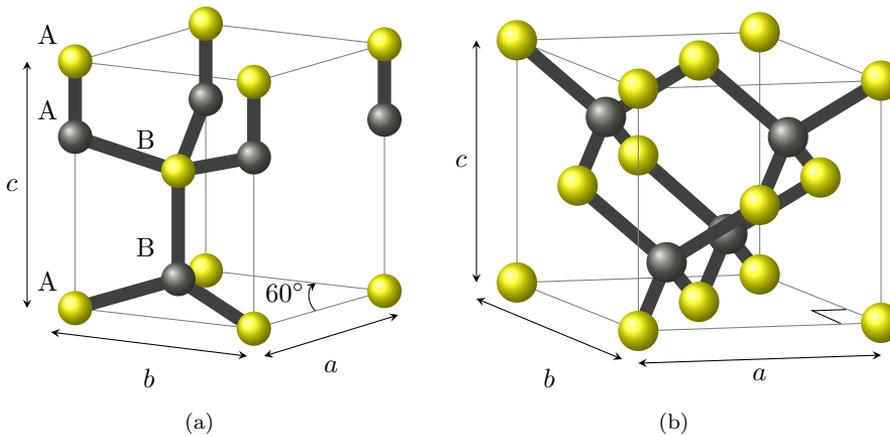
Figure 2.14: a) The hexagonal unit cell of wurtzite. Alternating layers of Zn and S in the [001] direction (along c) is forming a ABBABB stacking sequence. Yellow spheres represent sulfur atoms, gray represent zinc atoms. **b)** The cubic unit cell of zinc blende. The structure is a FCC lattice with two atoms in the basis where Zn ions are shifted $1/4$ of a_0 along the body diagonal with respect to the S ions. Yellow spheres represent sulfur atoms, gray represent zinc atoms.

diodes, tunable mid-infrared lasers [19] and second harmonic generation devices [20].

ZnS is a polymorphic material, meaning that it can form more than one crystal structure. The most common natural form is the cubic form, which has a bandgap of 3.7 eV [21]. This cubic form of ZnS is also known as sphalerite and zinc blende (referred to as zinc blende from now on), belongs to the space group F$\bar{4}$3m. Cubic ZnS has a face centered cubic (FFC) structure with two atoms in the basis with one atom in (000) and the other shifted $1/4$ along the body diagonal. Almost identical to the Si unit cell, the lattice parameter a_0 of zinc blende is 5.41 Å [22].

In addition to a cubic crystal structure, ZnS can also appear as a hexagonal wurtzite structure, belonging to the P6$_3$mc space group [23, 24]. The simple hexagonal close packed (hcp) lattice with one atom in the basis, has ABAB stacking in the [001] direction, where A and B are positions in the xy-plane. The wurtzite structure of ZnS (referred to as wurtzite from now on) is a hcp lattice with two atoms in the basis, seen in Fig. 2.14(a). This structure can be viewed as two intertwined hcp lattices, where the Zn lattice is shifted $5/8$ along the c-axis with respect to the S lattice. This gives a AABBAABB stacking sequence where the layers alternate between sulfur and zinc in the [001] direction. The lattice parameters of wurtzite are $a = b = 3.820$ Å and $c = 6.260$ Å [25].

The two crystal structures are related by composition and temperature according to the phase diagram in Fig. 2.15 [24]. αZnS and βZnS refers to zinc blende and

wurtzite respectively. L_1, L_2 and L_3 are ZnS liquids of different compositions. From the phase diagram it is seen that the zinc blende can transform to wurtzite at $1020\,^\circ$C when ZnS is stoichiometric [26].
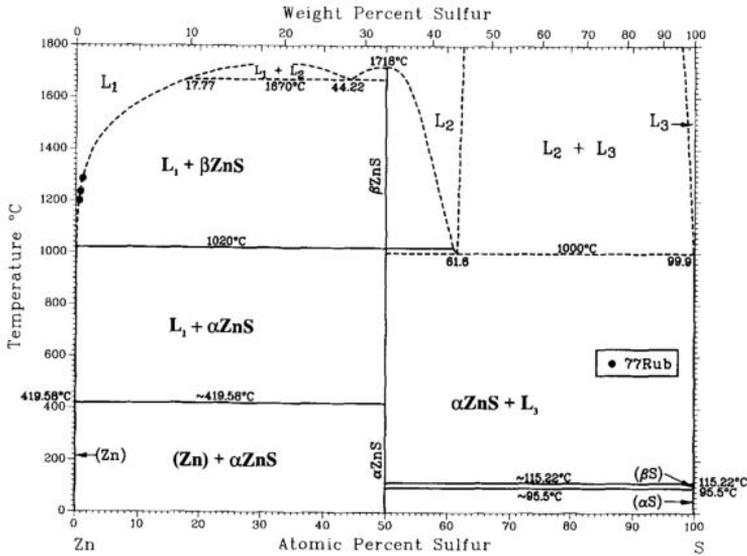

Figure 2.15: The phase diagram of systems consisting of Zn and S. Stoichiometric ZnS in its cubic form (αZnS) is the most stable and is transformed to hexagonal ZnS (βZnS) at $T = 1020\,^\circ$C. At different temperatures, ZnS forms mixtures of ZnS and liquids.

Chromium is number 24 in the periodic table and is a transition metal. Most of the commercial use of Cr is to form stainless steel, making use of the high corrosion resistance and hardness of Cr. Being a transition metal, Cr has a partially filled d-subshell. Due to this Cr can have a valence state from 0 to +VI which makes it a very versatile element. In the context of this thesis, Cr is used to make a band of energy states within the bandgap of ZnS. For this to happen the Cr should be evenly distributed in the film. There are essentially two ways for Cr to be incorporated in the ZnS lattice. One being that Cr is substituting Zn at a lattice point, and the other where it is incorporated interstitially in the lattice where there is no lattice point.

2.4   Thin Film Deposition Techniques

There are many different ways of depositing thin films both physically and chemically. This section will give a very brief overview of two commonly used techniques which are also used for producing the samples studied in this thesis.

2.4.1 Pulsed Laser Deposition

Pulsed laser deposition (PLD) is a physical vapor deposition technique for thin films first used in 1965 [27]. PLD is a versatile technique which can be used to deposit a range of different materials, high-temperature superconductors, semiconductors, oxides, nitrides and polymers to name a few [28]. Perhaps the most important property of PLD is its stoichiometric transfer of ablated material. [29, p.4-8].

The typical setup includes an ultrahigh vacuum chamber where the target material and substrate sits, and a laser capable of producing very short pulses, Fig. 2.16. Deposition is done by focusing the high powered laser at a target material to the point that it vaporizes. The evaporated material is in a plasma state and is visible as a plume normal to the target. This process is called laser ablation. High energetic ions in the plasma are ejected from the target and travels to the substrate through the vacuum chamber. The ions can then nucleate on the substrate and form thin films. The ablation process is very critical to film quality as ions with too high energy can sputter the film and substrate, causing defects in both.
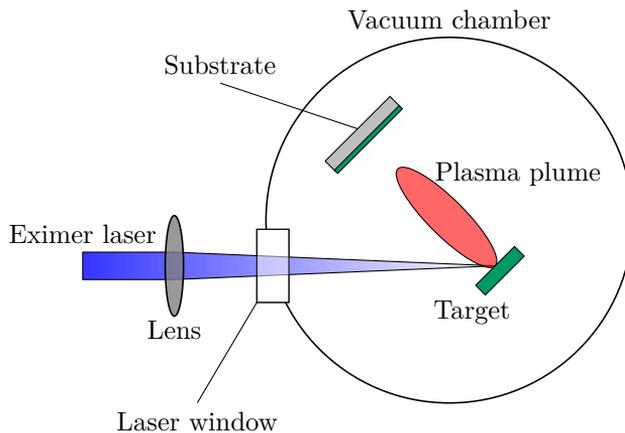
Figure 2.16: Schematic of a typical PLD setup. A focused pulsed laser ablates the target material in a vacuum chamber. The ablated material is deposited on the substrate.

2.4.2 Molecular Beam Epitaxy

Molecular beam epitaxy (MBE) is also a physical vapor deposition technique for thin films. The MBE technique has the capability of both depositing 2 dimensional layers of material and 3 dimensional islands. When mixing both, it is called

Stranski–Krastanov growth which is used for the quantum dot IBSC concept.

In MBE, each material deposited originates from its own source. This source is a Knudsen effusion cell, sometimes called a gun. The materials are heated until they are in their gas phase. Beams of the constituent materials are then directed towards the substrate using shutters to control the flow. MBE has its advantage in epitaxial crystal growth which means that the deposited material grows in the same crystal orientation as the substrate it is deposited on. Using slow growth rates ($\leq 1\,\mu$m/h), it is even possible to control layers at the monolevel, depositing one layer at a time [30, p.23-25]. This allows very small layered constructions to be made, and because of this MBE is sometimes called atomic spray paint. The MBE setup is illustrated in Fig. 2.17.
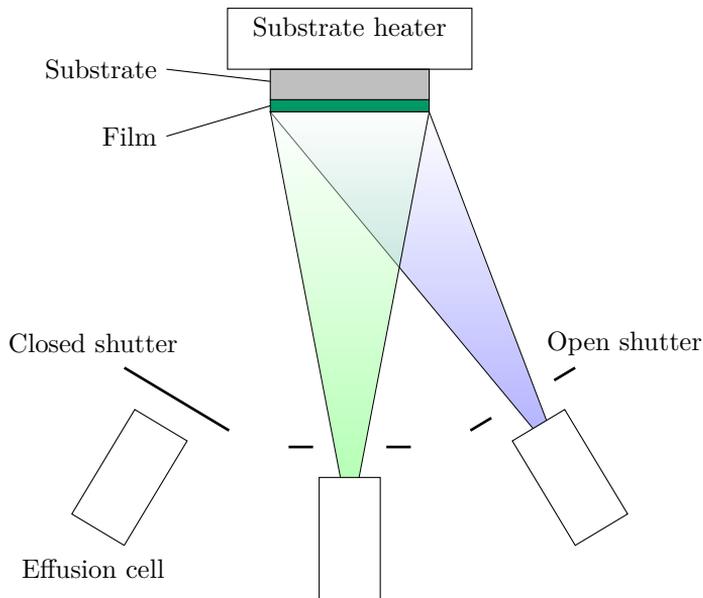

Figure 2.17: Schematic of a MBE. Each effusion cell contains an element which is heated into gas form. The gas diffuses to the substrate to deposit, and the shutters control the amount of each material into the mix.

Chapter 3

Experimental

This chapter gives an overview of the samples studied, experimental techniques and procedures used. The sample preparation and EELS analysis procedures are explained in detail as it is not too well documented in the literature.

3.1 Sample Overview

The samples studied in this thesis are Cr-doped ZnS thin films grown by PLD and MBE. PLD and MBE works differently and will give thin films with different microstructure and properties. Cr content, crystal structure, and grain sizes will vary depending on deposition techniques and growing parameters. All films were are deposited on a (100) plane of Si. Table 3.1 gives a list of the samples along with deposition technique, Cr concentration and specimen type, while Table 3.2 gives a detailed list of growing parameters. The following naming convention is used for the three samples, xZnS:Cry, where x is the first letter in the deposition technique, either P (PLD) or M (MBE). y signifies whether the sample was prepared as a cross section (CS) or plan view sample (PV). The convention is used to refer to samples without forgetting which sample is what and how it was prepared. Most emphasis has been put on comparing two cross section samples grown, MZnS:CrCS and PZnS:CrCS. The two PLD samples were not deposited at the same time, morphological differences between the two are therefore expected.

Table 3.1: Overview of the samples studied.

Deposition technique	at.% Cr [1]	Specimen type	Sample ID
MBE	1.5	Cross section	MZnS:CrCS
PLD	4 [2]	Cross section	PZnS:CrCS
PLD	4	Plan view	PZnS:CrPV

Table 3.2: Parameters for sample deposition.

Parameter	PZnS:CrCS	PZnS:CrPV	MZnS:CrCS
Substrate temperature [°C]	550	600	200
Base pressure [Torr]	$7.5 \cdot 10^{-8}$	$7.5 \cdot 10^{-8}$	$2.0 \cdot 10^{-8}$
Target-substrate distance [cm]	8	7	8
Ar background pressure [Torr]	$0.675 \cdot 10^{-3}$	$2.25 \cdot 10^{-3}$	-
Laser wavelength [nm]	248	248	-
Pulses per second [Hz]	5	5	-
Comcell temperature [°C]	-	-	982
E-beam power [W]	-	-	45
Deposition rate [Å/s]	-	-	0.6

3.2 The Microscopes

Three different TEMs have been used to study the three samples. A JEOL 2100 TEM equipped with a LaB_6 electron source and a Gatan 2k Orius CCD specifically designed for diffraction work has been used for low magnification BF imaging and diffraction work, while a JEOL 2100F field emission gun (FEG) TEM with a Gatan 2k UltraScan CCD was used for BF imaging and HRTEM. A high end double aberration corrected JEOL ARM200F, operated by SINTEF researcher Per Erik Vullum, has been used for an in depth study of the PZnS:CrCS sample by HRTEM, HAADF, EDX and EELS. The ARM200F is equipped with a cold FEG giving a high spatial and energy resolution, Centurio silicon drift detector EDX and Quantum Gatan Imaging Filter system with dual EELS capabilities. The data was collected by doing line scans perpendicular and parallel to the substrate interface in STEM mode. Low loss and high loss EELS spectra, EDX spectrum and HAADF were all recorded at the same time for all line scans. All TEMs are operated at an acceleration voltage of 200 kV and with an estimated error of 10% on the scale bars.

---

[1]Measured with Rutherford backscattering spectroscopy [31].
[2]Not measured with Rutherford backscattering, but reported by [31].

3.3 Sample Preparation

A TEM sample must fulfill two requirements. The sample must fit in the TEM sample holder and the areas of interest must be electron transparent. The thickness required to achieve electron transparency depends on the atomic number of the sample and the beam energy [13, p.11]. In order to get high quality high resolution images the thin parts of the sample should be in the order of 10 nm.

There are several ways of making TEM samples. Some methods are better suited for certain materials, and gives a specific specimen geometry. The samples studied are made by using the dimpling and ion milling route although other methods of specimen preparation have been explored. A finished cross section TEM specimen will look like a 3 mm wide disc with a spherical cap pit which has a hole in the bottom as seen in Fig. 3.3. The following text explains the method used for specimen preparation.

First the sample material is cut into 0.4 mm x 0.8 mm strips using a Testbourne Model 650 Diamond Wheel Saw equipped with a 150 μm Allied High Tech Wafering blade. This is done by heating a glass plate on a Framo Gerätetechnik M21 hot plate to about 125 °C. Wax is then melted on the glass and the sample is placed film side down on the wax. When the glass piece is taken off the hot plate the wax will harden and the sample is secured. The glass piece is mounted on the diamond saw and the sample is cut.

The strips are cleaned in a beaker of acetone to dissolve the remaining wax and then in a beaker of ethanol to remove acetone remnants. The strips lie in each beaker for about 5 minutes before gluing them together. Doing this forms a substrate-film-film-substrate "sandwich" as seen in Fig. 3.1. Allied High Tech EpoxyBond 110 is used for gluing the sandwich together. The glue is a mixture of 1 part hardening and 10 parts resin. A small amount is applied on both strips with a wooden toothpick. The sandwich is then put in a clamp and left on a hot plate for 30 minutes in order to cure the glue.
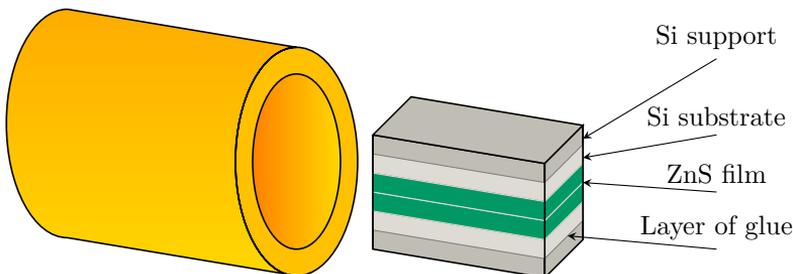

Figure 3.1: Schematic of the substrate-film-film-substrate sandwich and the brass tube. The shape of the sandwich is usually not rectangular.

The next step is to fit and glue the sandwich into a 3 mm hollow brass cylinder as in Fig. 3.1. Using a Struers RotoPol-21 grinding machine equipped with a SiC Grit P2500 grinding paper, the sandwich is ground to fit into the brass cylinder with inner diameter of 2 mm. When the sandwich has the correct dimensions, the cylinder is glued vertically on top of a small piece of Si wafer and filled with EpoxyBond 110. The sandwich is then inserted into the cylinder and is left on the hot plate for 30 minutes to cure the glue.

Next, the cylinder is mounted in the Diamond Wheel Saw and is sectioned into discs with a thickness of 1 mm. The discs are inspected and the disc with the least amount of damage from sawing is mounted on a clean dimpling stub. The stub is cleaned by grinding with Grit P2500 grinding paper until the surface is smooth. Then the stub is heated on a hot plate to about 125 °C, and the disc is fastened on the stub using a very small amount of wax. When the wax has hardened the disc is polished on the grinding machine with Grit P1200/2500/4000 papers until the surface is as smooth as possible. The stub is then heated in order to flip and grind the other side of the disc. Grinding is continued until the thickness of the disc is about $80 - 90\,\mu$m. The thickness is measured using a calibrated Olympus BX60 visual-light micoscope.
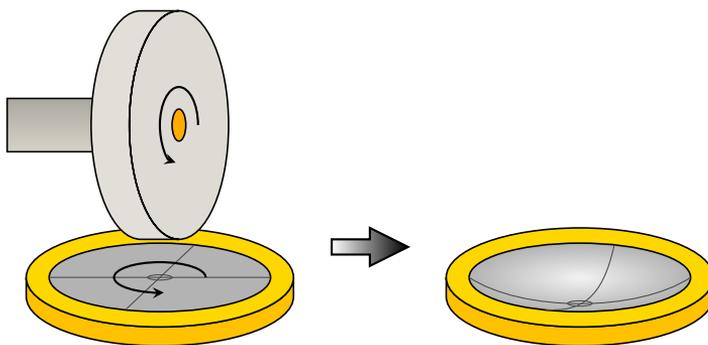

Figure 3.2: A rotating grinding wheel is carefully lowered while the stage is rotating the specimen to make the dimple. A mixture of distilled water and $1\,\mu$m Allied High Tech Polycrystalline Diamond Compound paste ensures gentle grinding. The gray lines only illustrate the topology of the sample, not glue lines, although they are noticeable under a VLM.

A spherical cap pit called a dimple is then made using an EAF Instruments Model 2000 dimpler as seen in Fig. 3.2. The machine is set to dimple a pit of $55 - 75\,\mu$m depth, leaving the thickness in the bottom of the pit around $20 - 25\,\mu$m. A grinding rate of $1.5\,\mu$m/min is used halfway through the depth of the dimple. A slower rate of $1\,\mu$m/min is used for the second half in order to reduce stresses on sample as cracks are easily made at this stage. $1\,\mu$m Allied High Tech Polycrystalline Diamond Compound mixed with distilled water is used as grinding lubrication. The specimen is now very thin and fragile, and is therefore

to be handled with extra care. The stub, still containing the specimen is put in a beaker of acetone to dissolve the wax, and thus releasing the specimen. Afterwards the specimen is cleaned in ethanol for about 5 minutes.

The last stage of preparation is to use a Gatan Precision Ion Polishing System Model 691 (PIPS) to sputter a hole through the bottom of the dimple using argon ions as seen in Fig. 3.3. The specimen is cooled using liquid N_2 during the sputtering process. First the specimen is inserted in a special holder for the PIPS with the glue layer between the thin films parallel to the holder clamps. The holder is then inserted into the PIPS vacuum chamber and milled by two opposing argon beams angled at 4° relative to the sample until there is a small hole in the bottom of the dimple. An acceleration voltage of 4 eV is used to start out with. As the Si substrate is getting thinner, a bright orange color is seen. This is an indicator that the specimen is almost penetrated. When the hole is achieved, the acceleration voltage is gradually decreased over 1 hour. In the end the acceleration voltage is 1 eV. A downside of ion milling is amorphization of the specimen . By gradually lowering the voltage, the thickness of the amorphous layer is minimized.
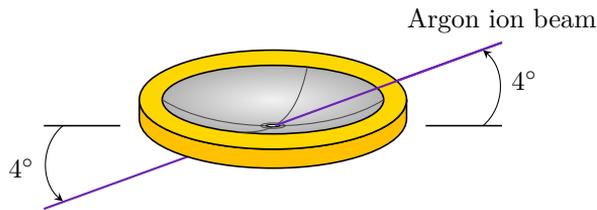
Figure 3.3: The specimen is subjected to argon beams sputtering a hole in the centre at a 4° angle from each side of the specimen. The gray lines only illustrate the topology of the sample, not glue lines, although they are noticeable under a VLM.

The specimen is now a finished TEM sample. Afterwards the specimen is inspected with a optical microscope where thickness fringes should be visible along the edge of the hole. One of the PLD sample was prepared as a plan view specimen. The plan view geometry is different from the cross section, but the preparation method is very similar, Fig. 3.4.
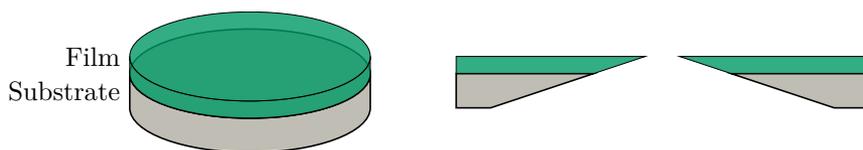
Figure 3.4: The plan view geometry after disc cutting (left) and the cross section view after ion milling when the specimen preparation is complete (right).

The preparation method used for plan view specimen is as follows. First, the sample material is cut into a disc with a diameter of 3 mm. This is done by using a Fischione Ultrasonic Disk Cutter Model 170 in continuous mode. The sample is waxed film side up on a glass plate, using the same wax and glass as before, and then mounted in the disc cutter. The disc cutter uses a very thin-walled cylinder vibrating at 26 kHz to cut out the disc. A force from the cylinder is acting on the sample at all times during cutting. A mixture consisting of 1200 grit SiC powder and distilled water is used to ensure that the cutting is as gentle as possible.

The sample is then released from the glass using the same acetone and ethanol procedure described above. Next, the disc is thinned and dimpled exactly like the cross section specimen, but with the film side facing against the stub. The final step is using the PIPS to make a small hole in the middle of the disc. The disc is mounted film side up in the PIPS holder, and the two ion cannons are both directed at 4° from below. This means that the surface of the thin film is never sputtered. Otherwise the PIPS procedure is the same as before.

3.4 Imaging and Diffraction

BF and diffraction imaging have been done along the [110] zone axis in Si on the two cross section samples, PZnS:CrCS and MZnS:CrCS. For the plane view sample, the Si [100] zone axis was used. The zone axes are decided by specimen preparation and sample geometry.

3.4.1 Crystal Structure Determination

The determination of the crystal structure of the Cr-doped specimen are done in Gatan Digital Micrograph (DM) [32] in conjunction with two useful scripts written by David Mitchell [33, 34]. First, a diffraction pattern is recorded for each specimen using a camera length of 200 cm to minimize noise between the reflections. By including the Si substrate with known d_{hkl}-values in the recording, the diffraction pattern has an internal calibration. Pixel coordinates of the center of the (000) reflection are then input in a script that defines the center of the image. The next script will use this center to rotationally average the

diffraction pattern. This improves the signal to noise ratio, useful for polycrystalline specimen with faint or incomplete ring patterns. The script also outputs a 1 dimensional line profile, making it easy to read which d_{hkl}-values that are present in the diffractogram after calibrating the plot.

Calibration to the Si substrate has to be done manually, and is easy to implement in a spreadsheet software or Python. Si has a cubic crystal structure which follows the simple relation between (hkl) indices and d-values,

$$d_{hkl} = \frac{a}{\sqrt{h^2 + k^2 + l^2}} \tag{3.1}$$

where a is the lattice parameter of Si. The length of the reciprocal lattice vector $|\boldsymbol{G}_{hkl}|$ for the Si (200) reflection is measured in pixels from the diffraction pattern N_{px}. Then, $|\boldsymbol{G}_{hkl}|$ is related back to d_{hkl} in the following manner

$$|\boldsymbol{G}_{200}^{Si}| = \frac{2\pi}{d_{hkl}} = \frac{4\pi}{a} = N_{px}^{200}, \tag{3.2}$$

which gives the length of a pixel in reciprocal space

$$L_{px} = \frac{4\pi}{N_{px}^{200} \cdot a}. \tag{3.3}$$

The distance between crystal planes in real space can now be expressed in terms of pixels in reciprocal space

$$d_{hkl} = \frac{2\pi}{|\boldsymbol{G}_{hkl}|} = \frac{2\pi}{N_{px}L_{px}}. \tag{3.4}$$

Plotting the intensity from the line profile versus Eq. (3.4) taking in N_{px}, gives a calibrated line profile for the rotationally averaged diffraction pattern which are in units easily comparable to X-Ray diffraction (XRD).

3.5 Spectroscopy

3.5.1 Quantification of Elements

EDX line scans are used for quantification of Zn, S and Cr in the sample. A Cliff-Lorimer routine in DM is used to quantify the elements [32]. The software provides the sensitivity factors.

3.5.2 Cr Valence State Determination

The EELS analysis is carried out using DM and an original script written in Python to determine the valence state of Cr [32]. The script is included in

Appendix A. The valence state of Cr is investigated by analyzing the Cr-$L_{2,3}$ fine structure. Since Cr is an element that can take valence states ranging from 0 to VI+, one parametrization of the Cr-$L_{2,3}$ fine structure is not enough for unambiguous determination of the Cr valence state [35]. Two parameters are therefore used, one being the ionization edges L_3 and L_2, and the other the ratio of the area under each ionization edge, hereby referred to as L_3/L_2 for brevity.

The background signal is first removed from the spectrum to isolate the signal from the fine structure before measuring the two parameters. Three features of the background signal must be subtracted, an exponential decaying tail from the plasmon peak in the low loss spectrum, a plasmon peak post fine structure due to multiple inelastic scattering, and the tail of L_3 into L_2. These three corrections are done in two steps, the first in DM and the second in Python using an original script. The paper by Daulton and Little [35] includes reference EELS data of Cr compounds spanning over the whole valence range of Cr. The corrections to the signal are done following the explanation in the reference paper in order to make the results comparable to the results given by Daulton and Little. Theoretical values for ionization edges and L_3/L_2 as a function of valency does not exist, values from literature is therefore needed. The method is as follows.

Extraction of the plasmon peak tail before the fine structure is removed by fitting it to a power law. The operation is done with an EELS software package in DM. The measured high loss signal can be viewed as a convolution between the ideal high loss spectrum with the low loss signal [17, p.700]. A deconvolution of the two spectra yields a high loss signal without the effects of multiple scattering. The deconvolution routines in DM can add a lot of noise to the fine structure signal. A low pass filter is therefore used to smooth out the signal. The effects of the power law fitting, deconvolution and smoothing are shown in Fig 3.5.

The tail of the L_3 fine structure is removed by using a two-step model implemented in Python as described in [35], shown in Fig. 3.6. The height of the rightmost black line is the mean value of the signal within a 2 eV window starting 4.8 eV from the L_2 fine structure edge, shown as vertical dashed line. The ratio of the two steps should be the same as the L_3/L_2 ratio. Since this ratio is not yet calculated at this point, an initial value of 2 is used, meaning that the left step is twice as big as the right. The initial value of 2 is chosen as a first-order approximation, which is consistent with the electron configuration of Cr, four $2p_{3/2}$ electrons and two $2p_{1/2}$ electrons in the 3d-orbital. The step ratio is then refined by iteration until $\Delta L_3/L_2 \leq 10^{-5}$ which completes the background subtractions.

The edge of L_3 and L_2 are measured after smoothing of the signal. This is done by measuring the FWHM and selecting the channel in the middle as the edge. Then the ratio L_3/L_2 is calculated by integrating over a 5 eV wide window centered on each of the edges as shown in Fig. 3.6.
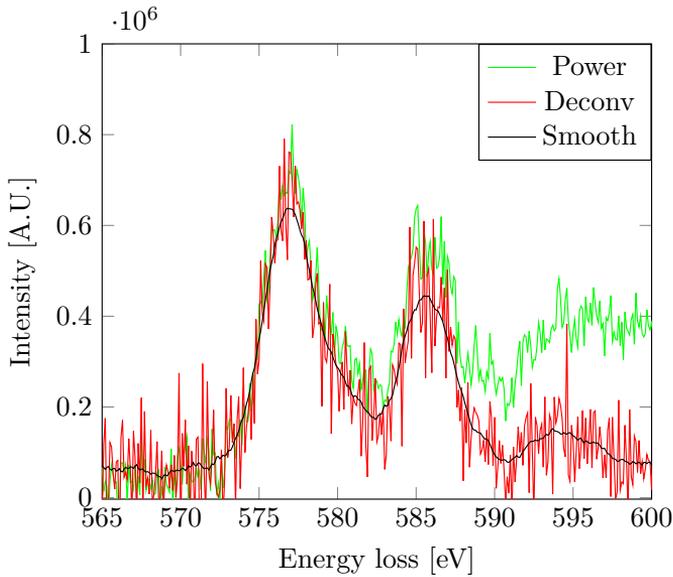
Figure 3.5: The Cr-L$_{2,3}$ fine structure signal when the first plasmon peak tail is removed (power, green), when also multiple scattering is removed (deconv, red) and after smoothing the red curve (smooth, black).
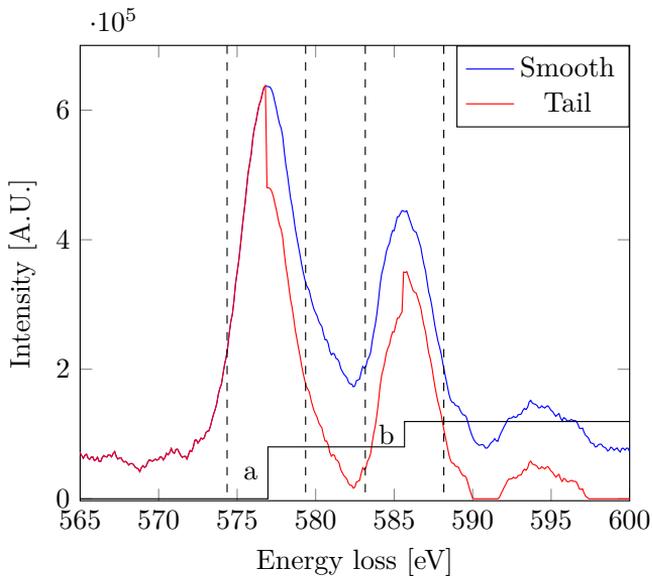
Figure 3.6: The Cr-L$_2$, 3 fine structure before the tail of L$_3$ in L$_2$ is removed (blue, smooth) and after (red, tail). The two-step function (black) is subtracted from the blue curve. The vertical dashed lines show the limits of integration used when calculating L$_3$/L$_2$.

Chapter 4

Results

This chapter presents the results starting on a large scale with the morphology of the film, diffraction and crystal structure, and ending with the spectroscopy analysis. The reader is reminded that three samples have been studied and that the naming convention given in Table 3.1 contains information about which deposition technique and preparation method was used. All BF and HAADF images are rotated so that the growth direction is pointing upwards unless otherwise is stated in the figure caption.

4.1 Film Morphology

4.1.1 Grain Structure and Size

The shape and size of grains have been examined using BF images. Grain size will refer to the width of the grains through the rest of the text. Diffraction contrast reveal grains in different orientations. This gives clear grain boundaries so that the size of the grains can be measured. Table 4.1 summarizes the findings on grain size from the samples. More in-depth results from the individual samples are presented in the following subsections.

Table 4.1: Grain width from PZnS:CrCS, PZnS:CrPV and MZnS:CrCS

Sample ID	Average size [nm]	σ [nm]	# grains
PZnS:CrCS	27.3±1.8	8.5	23
PZnS:CrPV	38.2±1.6	14.9	89
MZnS:CrCS	26.5±1.7	8.0	24

PZnS:CrCS

The cross section PLD sample shows columnar grain structures, evident from Fig. 4.1(a). The grains can extend from the substrate to the film surface or stop somewhere in between, as seen in Fig 4.1(b). Evidence of Van der Drift growth can be seen close to the substrate interface, as the grains are starting out small and increases in width through the film [36]. Fig. 4.2 shows how the grains starts out with a needlelike shape at first and how it expands as the film grows.


(a)   (b)
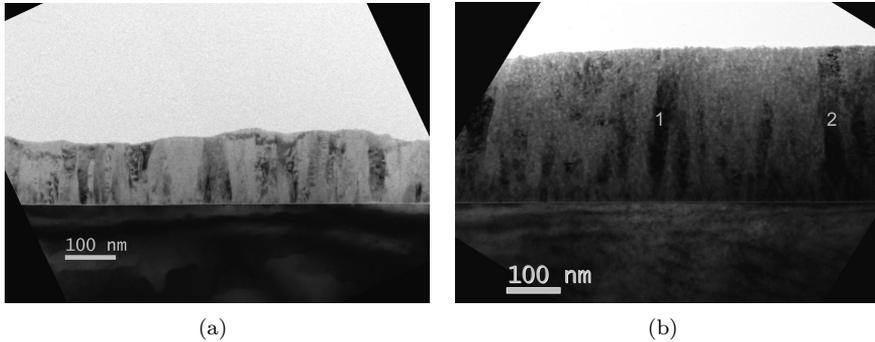
Figure 4.1: a) BF image of PZnS:CrCS. Columnar grains can be seen due to diffraction contrast and the width can be measured. **b)** BF image of PZnS:CrCS. Grains annotated as 1 and 2 are examples of van der Drift growth. The grains have a neeedle-like structure at the interface and expands as the film grows.

The grains vary from 15-45 nm in size with an average size of 27.3±1.8 nm. The standard deviation σ for the 23 grains examined is 8.5 nm. Diffraction images reveals a polycrystalline film with strong ring patterns, shown in Fig. 4.3(a). A texture along the direction of the film is seen below the (200) Si reflection. The group of reflections, denoted a) in the figure, under the Si (200) reflection belong to the (111) planes of zinc blende or the (200) planes of ZnS in the wurtzite form. The Fourier transform of grains that have been atomically resolved show crystals in either the cubic [111] direction or the hexagonal [001] direction, as illustrated in Fig. 4.4.

This sample has also been prepared as a single hetero-junction solar cell and tested [37]. An efficiency of 0.28% with $I_{sc} = 2.73 \, \mathrm{mA/cm^2}$, $V_{oc} = 0.32 \, \mathrm{V}$ and a fill factor FF = 0.32 was reported.
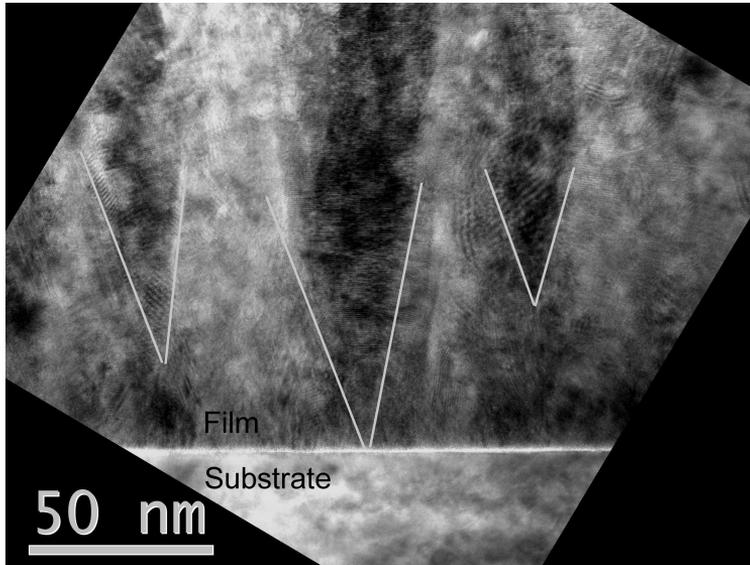
Figure 4.2: BF image of van der Drift grains in the PZnS:CrCS sample near the substrate. The gray lines show the expanding nature of the grains through the film. Thickness variations due to specimen preparation gives uneven contrast, making white dots appear.
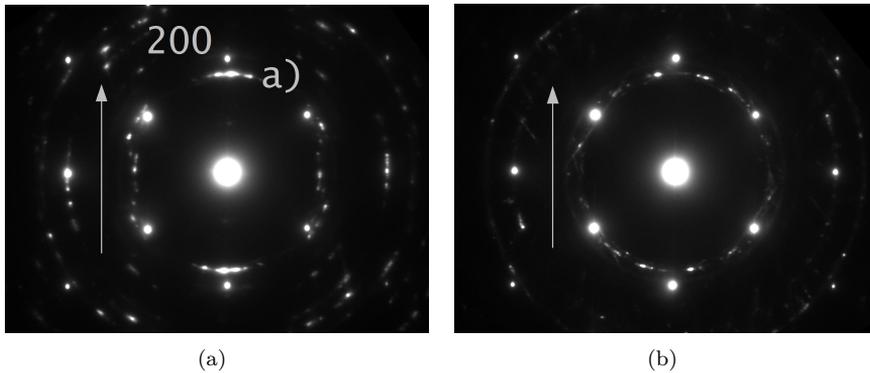
Figure 4.3: a) Diffraction image of PZnS:CrCS. Strong ring patterns shows that the sample is highly polycrystalline with a (111) zinc blende or (200) wurtzite texture along the growth direction. **b)** Diffraction image of MZnS:Cr. Strong ring patterns show that the sample is highly polycrystalline without a clear texture. The arrows in both images are perpendicular to the substrate interface in the direction of growth.
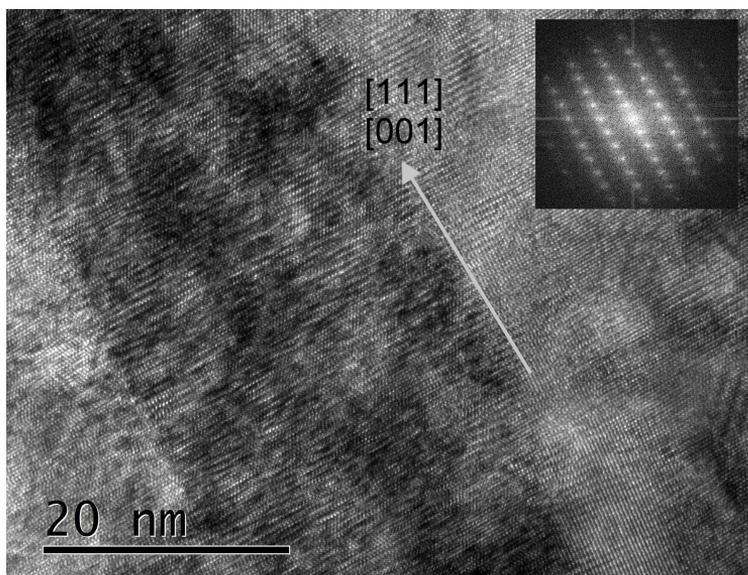
Figure 4.4: HRTEM image of the PZnS:CrCS sample showing a grain in the zinc blende [111] direction or the [001] direction in wurtzite. This is the same as the growth direction as the arrow indicates.

PZnS:CrPV

The PLD sample prepared to be studied in plan view gives a different perspective on the shape of the grains. From the top down view it is seen that the grains have an irregular shape, Fig. 4.5(a). Some of the grains have very defined edges which are facets which is another feature of Van der Drift growth. HRTEM images show grains oriented in either the [111] direction of zinc blende or the [001] direction of wurtzite, Fig. 4.6. The size of the grains vary from 14-72 nm, with an average grain size of 38.19±1.6 nm. The standard deviation σ for the 89 grains examined is 14.9 nm. Diffraction images show that the grains are oriented in all directions, Fig. 4.5(b).

MZnS:Cr

The MBE sample also shows that grains grow in a columnar fashion through the thickness of the film, Fig. 4.7(a). The grains vary from 11-44 nm in size with an average size of 26.5±1.7 nm. The standard deviation σ for the 24 grains examined is 8.0 nm. Evidence of Van der Drift growth is seen, Fig 4.7(b). Large amounts of stacking faults are found in the grains, Fig. 4.8. These stacking faults are

(a)   (b)
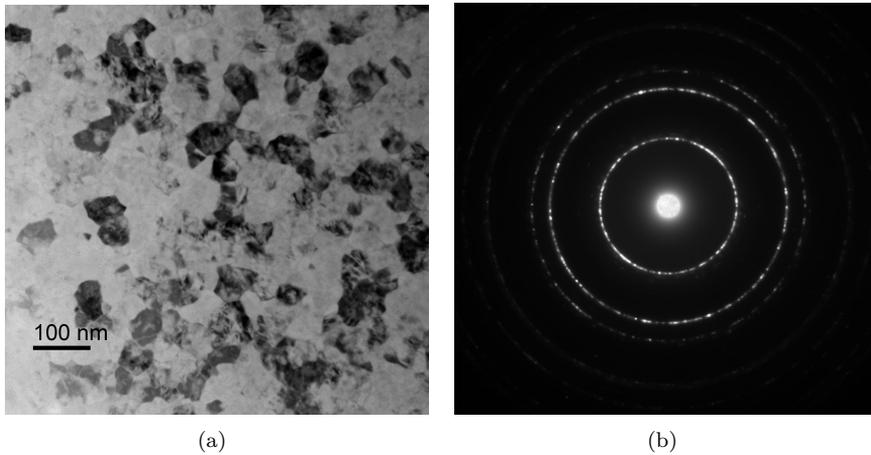
Figure 4.5: a) BF image of PZnS:CrPV. The grains in all sorts of shapes are seen. Some grains are faceted. **b)** Diffraction pattern of PZnS:CrPV. The grains are oriented all ways which results in complete rings for each reflection. As expected there is no texture.
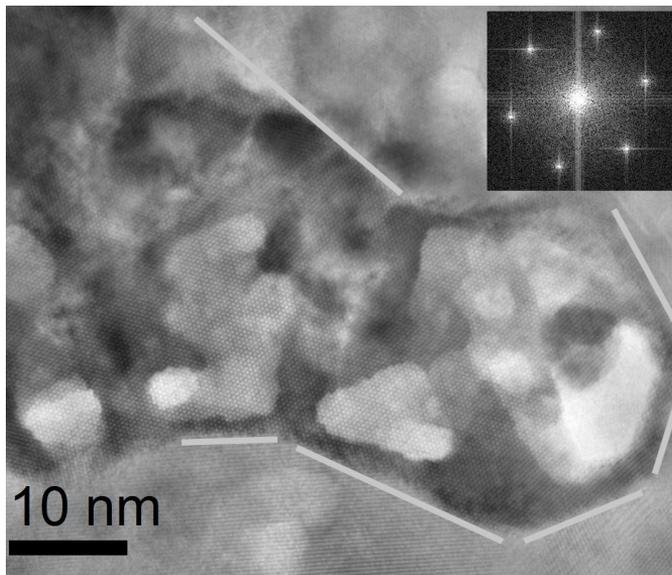
Figure 4.6: HRTEM image of a grain in the PZnS:CrPV sample showing a 6-fold symmetry. The grain is either a zinc blende grain seen from the [111] direction or a wurtzite grain from the [001] direction. The grain shows straight grain boundaries (gray lines) which indicate that it is faceted. The inset shows the 6-fold symmetry of the Fourier transform of the central grain.

(a)

(b)
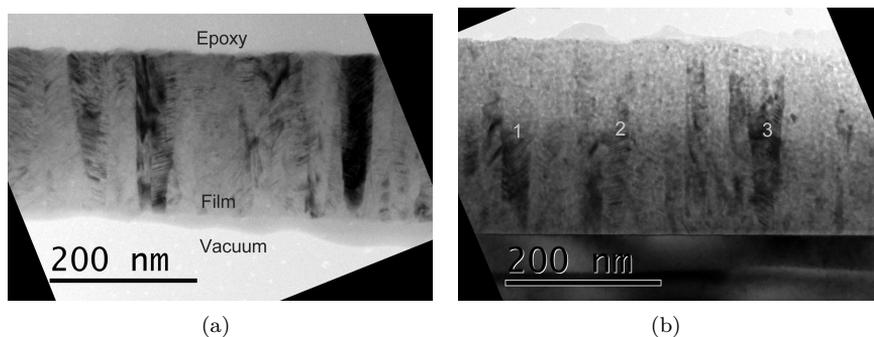
Figure 4.7: a) BF image of the cross section of MZnS:Cr. Columnar grains can be seen due to diffraction contrast and the width can be measured. **b)** BF image of the cross section of MZnS:Cr. Grains annotated 1 and 3 show Van der Drift growth. Stacking faults are visible as parallel lines along the grains 1, 2 and 3.

twin defects which form in the [111] direction in zinc blende [38, 39]. Diffraction images show strong ring patterns, meaning the film is polycrystalline and have grains in random orientations, Fig. 4.3(b). No clear texture is observed from diffraction images.
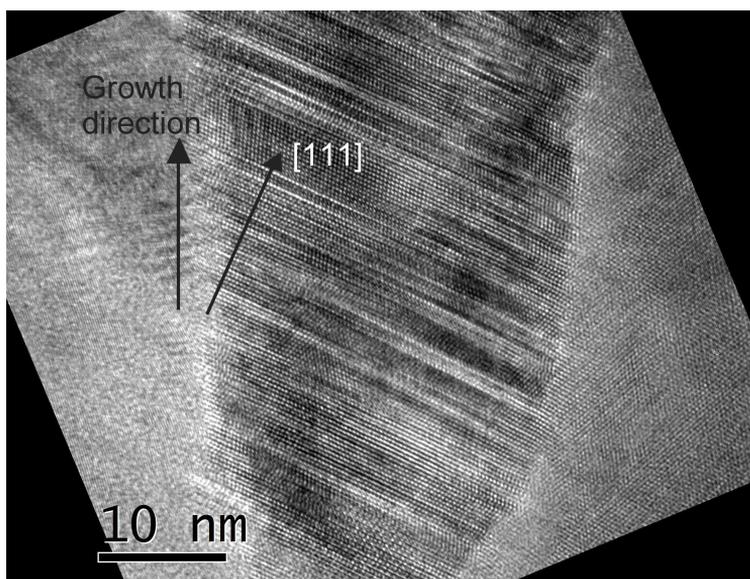
Figure 4.8: HRTEM image of stacking faults in a grain in the MZnS:CrCS sample. The cubic zinc blende structure forms twin defects in the [111] direction.

4.1.2 Crystal Structure

The crystal structure was investigated using diffraction images and the method described in section 3.4.1. The 1 dimensional intensity profiles in Fig. 4.9 show that the samples grown by PLD are different from the MBE sample. The two samples grown by PLD have several diffraction peaks that are unique to wurtzite ZnS. The MBE sample has only one peak that can be tied to the wurzite phase of ZnS. The d_{hkl} values that are unique to wurtzite ZnS are marked as vertical dashed lines in the Fig. 4.9. A complete summary of which reflections appear in each sample is found in Table 4.2, 4.3 and 4.4. The table includes theoretical d_{hkl} values for the suggested (hkl) reflections for each material.

Table 4.2: Possible (hkl) reflections with corresponding d_{hkl} values in zinc blende and wurtzite ZnS structures, in addition to Si present in MZnS:CrCS.

| Peak [Å]	Wurtzite [hkl/(Å)]	Zinc blende [hkl/(Å)]	Si [hkl/(Å)]
3.11	002 (3.11)	111 (3.12)	111 (3.12)
2.71	-	200 (2.69)	200 (2.72)
1.92	110 (1.90)	220 (1.91)	220 (1.91)
1.63	112 (1.62)	311 (1.63)	311 (1.63)
1.57	201 (1.59)	-	-
1.35	-	400 (1.35)	400 (1.35)
1.25	210 (1.25)	331 (1.24)	331 (1.24)

Table 4.3: Possible (hkl) reflections with corresponding d_{hkl} values in zinc blende and wurtzite ZnS structures, in addition to Si present in PZnS:CrPV.

Peak [Å]	Wurtzite [hkl/(Å)]	Zinc blende [hkl/(Å)]	Si [hkl/(Å)][1]
3.32	100 (3.29)	-	-
1.91	110 (1.90)	220 (1.91)	220 (1.91)
1.66	200 (1.65)	-	-
1.60	201 (1.59)	-	-
1.25	210 (1.25)	331 (1.24)	331 (1.24)

---

[1] No diffraction from Si is expected due to sample preparation removing the substrate under the thin film.
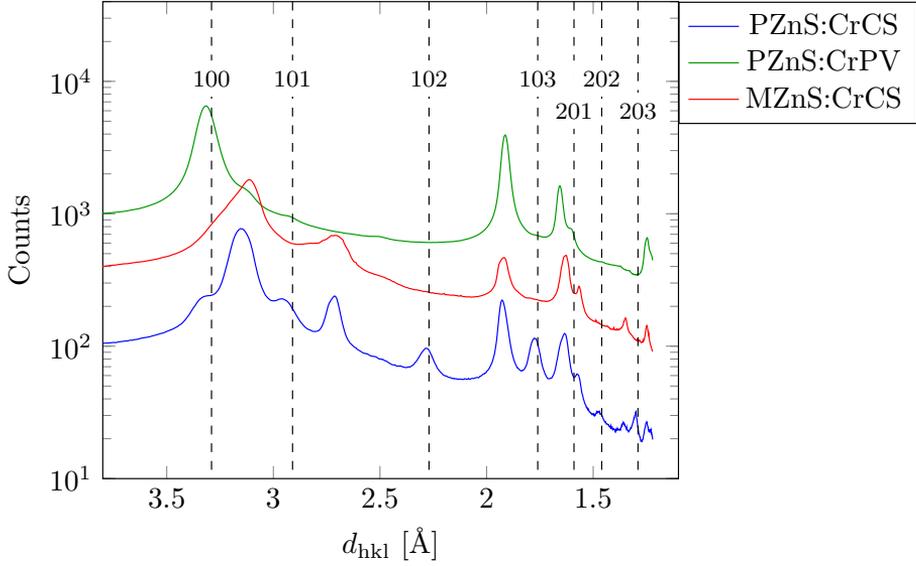
Figure 4.9: 1 dimensional intensity profiles generated by rotationally averaging diffraction images from the three samples. Vertical dashed lines denote d_{hkl} values associated with ZnS in the wurtzite phase.

Table 4.4: Possible (hkl) reflections with corresponding d_{hkl} values in zinc blende and wurtzite ZnS structures, in addition to Si present in PZnS:CrCS

Peak [Å]	Wurtzite [hkl/(Å)]	Zinc blende [hkl/(Å)]	Si [hkl/(Å)]
3.31	100 (3.29)	-	-
3.15	002 (3.11)	111 (3.12)	111 (3.12)
2.96	101 (2.91)	-	-
2.71	-	200 (2.69)	200 (2.72)
2.28	102 (2.27)	-	-
1.93	110 (1.90)	220 (1.91)	220 (1.91)
1.77	103 (1.76)	-	-
1.63	112 (1.62)	311 (1.63)	311 (1.63)
1.57	201 (1.59)	-	-
1.47	202 (1.46)	-	-
1.36	-	400 (1.35)	400 (1.35)
1.30	203 (1.29)	-	-
1.25	210 (1.25)	331 (1.24)	331 (1.24)

4.2   Spectroscopy

This section presents the findings from the two spectroscopy techniques used, EDX and EELS. Five line scans done on the PZnS:CrCS sample have been studied, two perpendicular to the substrate interface and three parallel to the interface. The PZnS:CrCS was selected to be studied in more detail due to high Cr content, and the quality of the specimen. EDX and EELS data was collected in each line scan. Line scan 1 and 2 are perpendicular to the substrate interface, while line scans 3 and 4 are in parallel close to the interface. Line scan 5 is parallel to the substrate but closer to the top of the film. A HAADF image was taken before every line scan, showing where the scan was done, shown in Fig. 4.10.

4.2.1   EDX

Five line scans have been used to investigate the distribution of Cr in the cross section PLD sample. Using EDX line scans it is possible to find out if the Cr is segregated to certain areas, precipitated or evenly distributed. The Kα lines of Si, Zn, S and Cr have been used for the analysis. Averaging the five line scans yield 4.41±0.03% Cr in the thin film. Table 4.5 summarizes the results of quantification from each line. Line scans perpendicular to the substrate interface show that there is no Cr at the interface, see Fig. 4.11. Cr signals are detected 1-4 nm from the interface. Large variations in Cr content are seen in all line scans, see Fig. 4.11, 4.13, 4.14 and 4.12. Peaks in the Cr signal are systematically accompanied with a decrease in the Zn concentration, while the fraction of S is constant. This is evidence for Cr substituting Zn in the ZnS lattice. Variations in Cr are the most pronounced in line scans done in parallel to the substrate interface. Scans show variations of 10% Cr within 10 nm.

Table 4.5: Cliff-Lorimer quantification of Zn, S and Cr from their Kα lines.

Scan #	Zn [at. %]	S [at. %]	Cr [at. %]
1	43.94±0.10	52.07±0.12	3.99±0.03
2	42.19±0.09	53.11±0.07	4.70±0.02
3	43.43±0.09	52.42±0.08	4.15±0.02
4	41.66±0.12	54.00±0.11	4.35±0.04
5	41.84±0.13	53.28±0.11	4.88±0.04
Average	42.61±0.11	52.98±0.10	4.41±0.03

(a)

(b)

(c)

(d)
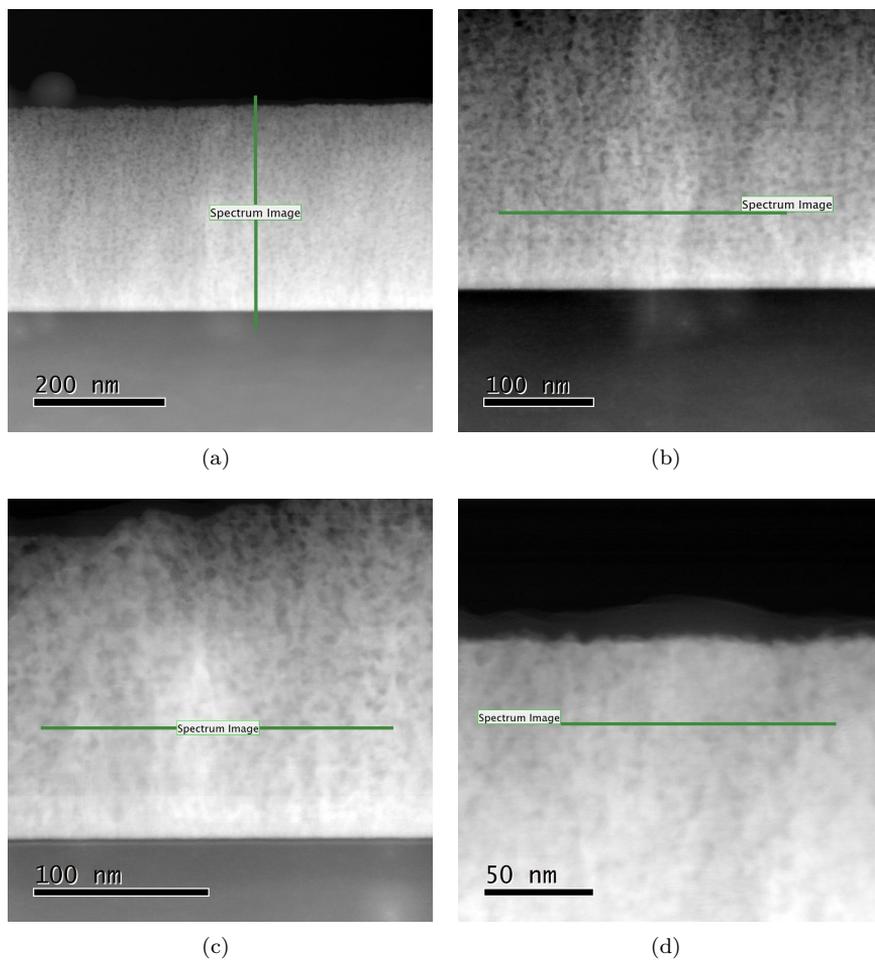
Figure 4.10: HAADF images showing which part of the film was scanned for line scans 2-5 in an ordered fashion.
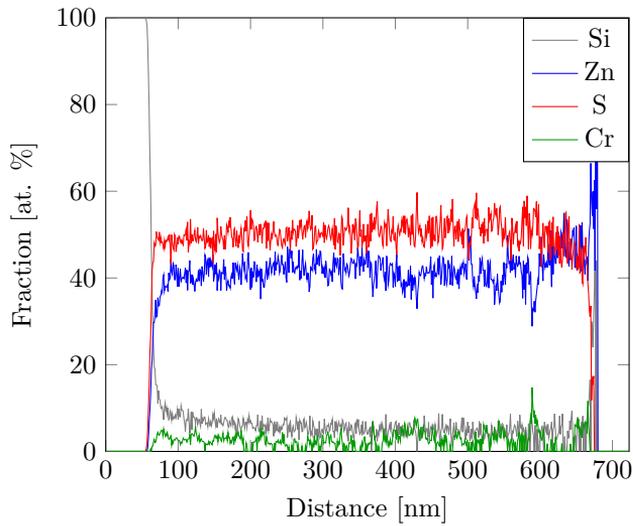
Figure 4.11: EDX line scan 1 of PZnS:CrCS perpendicular to the substrate. The Cr signal is delayed by a few nanometers from the interface indicating a band of ZnS without Cr at the interface. This band is 1-4 nm wide. Large variations in Cr content is seen. The Cliff-Lorimer method fails at 680 nm where there is no specimen.
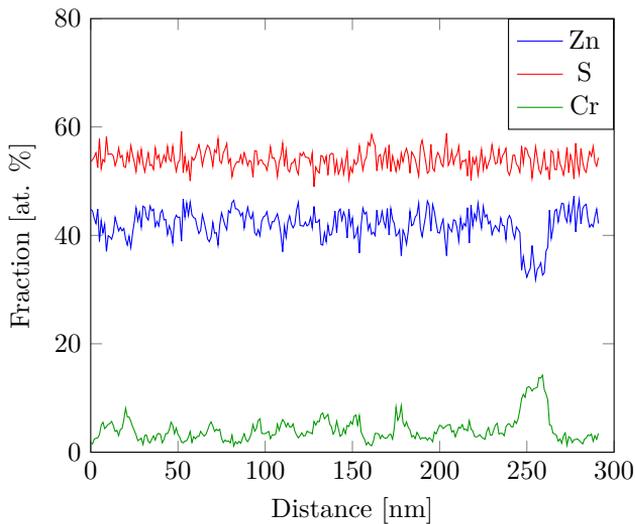
Figure 4.12: EDX line scan 5 of PZnS:CrCS parallel to the substrate. This scan was done close to the film surface. Large variations in Cr concentration are seen.
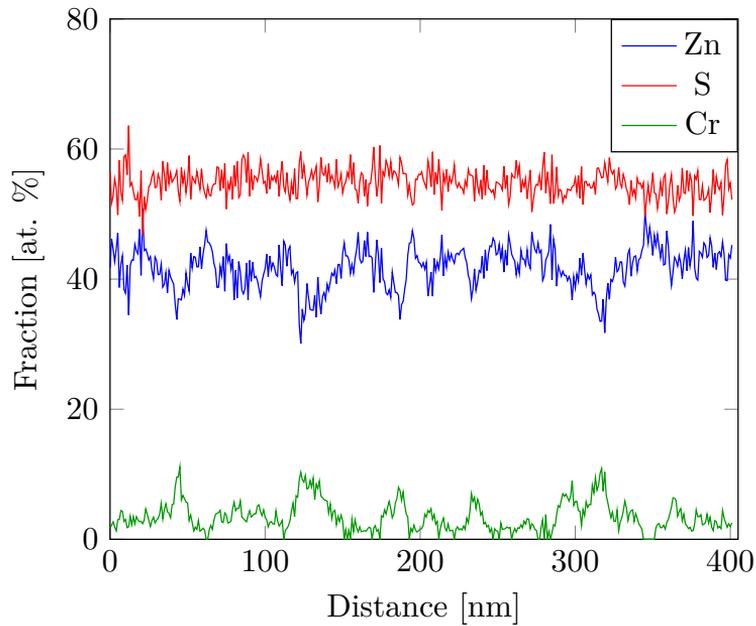
Figure 4.13: EDX line scan 4 of PZnS:CrCS parallel to the substrate. Cr and Zn varies opposite to each other while the S signal is constant, indicating that Cr substitutes Zn in the ZnS lattice. Cr contents vary from 1% to 11% within 10 nm.

4.2.2 EELS

EELS was used to investigate the integration of Cr in the ZnS thin films when the doping level is very high. The Cr-L_3 and Cr-L_2 edges have been determined and the ratio of the area under each edge L_3/L_2 has been calculated. From these results, the identification of the valence state of Cr has been determined to be +II. It has also been attempted to see if there is any variation in Cr valency from different parts of the thin film. The results from the investigation of different areas in the four line scans analyzed are presented in Table 4.6. The results are deduced by comparing the values in Table 4.6 to the tables in Fig. B.1 and B.2 in Appendix B. Each of the four scans are split in two, making the analysis treat the first and second half of each scan separately. The notation used in the "Scan #" column identifies the scan line 2-5 with a number 1-2, for the first or second half of the scan respectively. The energy resolution of the EELS data is 1 eV.

Scan 3 seen in Fig. 4.10(b) was scanned over a rather large grain with clear grain boundaries. The Cr-L edges vary in intensity over this grain, with a strong signal before the grain (region 1) and a weak signal in the grain (region 2), see HAADF in Fig. 4.14. The Cr-L edges were measured and L_3/L_2 ratio calculated for these two regions, and the result is included in Table 4.6. The EDX data from the same scan shows that there is a small amount of Cr between 200 and 300 nm, which is where the grain is, Fig. 4.14. Region 1 has a Cr peak in the EDX data.

Table 4.6: Cr-L edges and adsorption edge ratios.

Scan #	L_3 [eV] [2]	L_2 [eV] [2]	L_3/L_2	Valence state
2-1	576.9	585.6	1.8334	II
2-2	576.8	585.8	1.8704	II
3-1	577.1	586.0	1.6871	II
3-2	577.4	586.3	1.6142	II
3-left	577.0	586.0	1.8799	II
3-grain	577.4	586.3	1.6243	II
4-1	577.2	586.0	1.6641	II
4-2	577.4	586.2	1.6410	II
5-1	577.2	586.2	1.7714	II
5-2	577.4	586.1	1.7949	II
Average	577.2	586.1	1.7381	II

[2]All values have an uncertainty of ± 0.1 eV
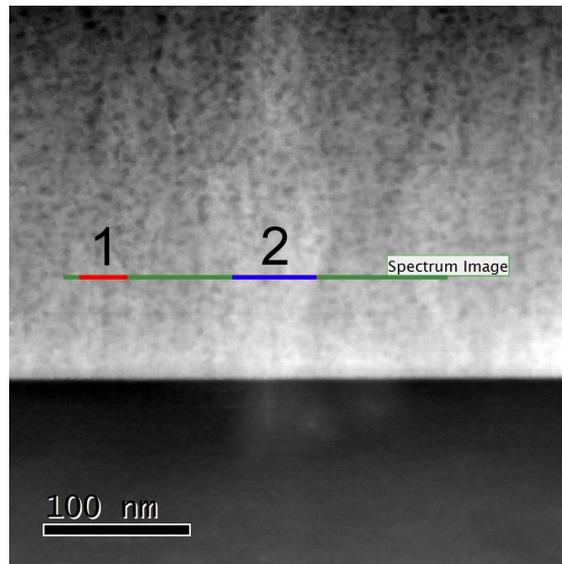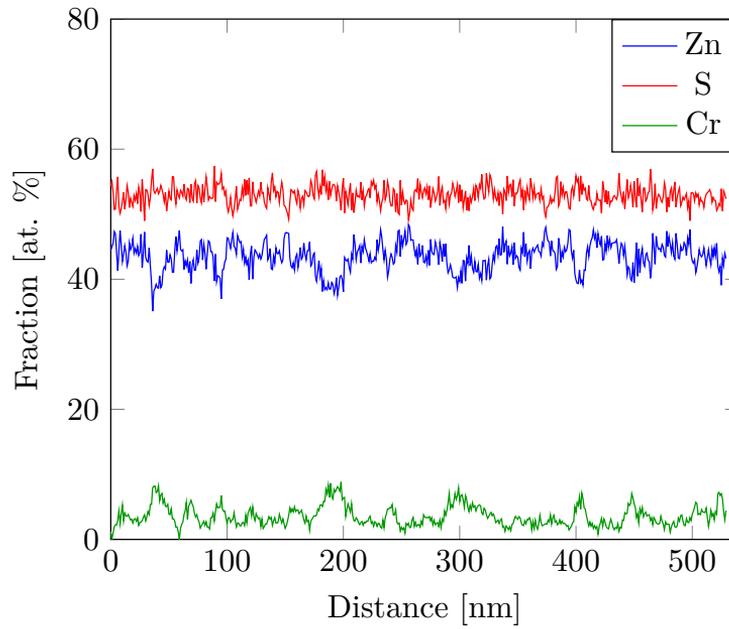
Figure 4.14: The plot shows the intensity difference of the Cr-L edges in region 1 and 2 which suggests a difference in Cr content. The L_3 fine structure has its peak at $577.0\,\text{eV}$ in region 1, while in region 2 the peak is at $577.4\,\text{eV}$. The HAADF image shows where region 1 and 2 are located on the scan line.

Chapter 5

Discussion

5.1 Film Morphology

5.1.1 Grain Structure and Size

The study of the grains in the three samples has shown that there are morphological differences and similarities between the samples. Common for the three samples are that they are all polycrystalline with grain widths in the nanometer range. This might be somewhat unexpected due to the lattice parameter of Si (5.43 Å) and zinc blende (5.41 Å) being so similar, thus being good conditions for epitaxial growth. The explanation of why there is no epitaxial growth lies in the details of competitive growth and surface energy differences in different crystal planes [40, 41]. The full explanation is not in the scope of this project and will not be discussed further. It is also possible that the presence of Cr affects the possibility of epitaxial growth. The reader is reminded that grain size refers to the width of the grain, which is parallel to the substrate interface.

The two cross section samples, PZnS:CrCS and MZnS:CrCS, show similar grain size and structure. Evidence of van der Drift growth is seen in BF images as V-shaped columnar grain structures [40]. The van der Drift growth model is a well established theory explaining the mechanics behind these structures, but is outside the scope of this work [41]. Due to the V-shaped grains, the size might be a little ambiguous. The result will vary depending on where in the thin film size is measured. The measurements were done at half of the film thickness for both cross section samples to have as comparable results as possible. Still, factors like film thickness and where the grains start will impact the size measured. An increase in film thickness will matter, since the grains can expand more before reaching halfway through the film, thus appearing bigger. Similarly, grains that start further from the substrate will appear smaller compared to those that start at the substrate.

The MBE sample is found to have grains with a high amount of stacking faults from HRTEM images, Fig. 4.8. These stacking faults are not seen in the PLD samples. This difference could be due to the Cr concentration being different or simply that different deposition techniques have been used. A feature found in the cross section PLD sample is that the crystallites have a preferred direction of growth, as shown in Fig. 4.3(a). This texture is normal to the substrate, and the planes aligning in that direction belong to the (111) planes in zinc blende or (002) in wurtzite. This texture is not found in the MBE sample. These features are discussed in greater detail in section 5.1.2.

In the case of the plan view sample, PZnS:CrPV, all grains were measured at the surface of the film due to specimen preparation. The average grain size was found to be 38.2±1.6 nm by measuring 89 grains. If the van der Drift growth model applies to this sample, it means that the grain size is probably smaller than they appear. If they were measured at half of the film thickness, it could be that the sizes were more similar to the average values of 27.3±1.8 nm and 26.5±1.7 nm for the cross section PLD and MBE samples, respectively. The difference in grain size between the two PLD samples could also be due to Cr concentration or different growth parameters being used. To validate the size measurements for this sample, the cross section should also be studied. This was not done due to material availability.

Grain size in crystals are often measured by various intersection methods where a line or circle is drawn, and the number of grain boundaries intersected are counted. A method like this is not possible on the samples studied since grain boundaries are often not visible. This would have lead to a larger grain size as not all grain boundaries would have been counted. However, there are also problems with measuring grain size visible only by diffraction contrast. Hypothetically, it could be that those grains are larger than grains not fulfilling the Laue condition in a certain zone axis. The results presented on grain size does not give the best accuracy based on the arguments above. The reported shape of the grains on the other hand, should be quite accurately described. A more detailed description could be achieved by preparing the samples to be studied from both perspectives. Again, this was not done due to material availability.

The morphological findings show that the samples have a lot of unfavorable properties for use in solar cells. Every imperfection in the film will act as recombination centers and decrease the efficiency of the cell. However, epitaxial growth of ZnS on sapphire and silicon substrates using PLD has been reported [26]. An epitaxial ZnS thin film should yield better conversion efficiencies than what has been achieved at this point.

5.1.2   Crystal Structure

Due to the polymorphism of ZnS, diffraction images were studied in detail to uncover the crystal structure of the thin films. The possibilities are one crystal

structure, either zinc blende or wurtzite, or a mixture of both structures. The crystal structure was investigated using the data from the 1D intensity profiles in Fig. 4.9 and Tables 4.2, 4.3 and 4.4. From these tables it is seen that samples grown by PLD, have their majority of peaks associated with wurtzite ZnS. The other peaks can originate from planes in the wurtzite or zinc blende structure because of similar d_{hkl} values. These peaks cannot be used to rule out one of the crystal structures.

Consequently, an unambiguous crystal structure cannot be determined by diffraction in TEM. This is the case as long as there are reflections with d_{hkl} values found in both crystal structures. A difference between PZnS:CrCS and MZnS:CrCS is, however, obvious. If the two samples had the same structure, their diffraction patterns and 1D intensity profiles would look the same. This is not the case. The MZnS:CrCS sample shows only one reflection associated with wurtzite, while PZnS:CrCS shows seven. This can mean two things, either that the MBE sample is mostly zinc blende with a small amount of wurtzite, or that the grains in the MBE sample is oriented so that any wurtzite reflection other than (201) fulfills the Laue criterion. Both are possible explanations.

The HRTEM images of both PLD samples show grains that are either the [111] zinc blende direction or the [001] wurtzite direction. An illustration of this can be found in Fig 4.4, 4.6. The Fourier transform inset shows that both are possible. In Fig. 4.4, the Fourier transform could show a rectangular pattern from a wurtzite structure imaged along the [110] zone axis, oriented in the [001] direction. It could also show a zinc blende structure imaged along the [11$\bar{2}$] zone axis, oriented in the [111] direction. A similar argument explains the HRTEM image of the plan view sample. The hexagonal pattern in the Fourier transform in Fig. 4.6 could be a zinc blende structure imaged along the [111] zone axis or a wurtzite structure along the [001] zone axis. Both would yield a pattern with 6-fold symmetry. A tool simulating kinematical diffraction was used to find out how diffraction patterns of zinc blende and wurtzite structures in certain directions should look like [42].

The high density of twin defects in Fig. 4.8 indicate formation of zinc blende grains, as they are known to form these defects [38, 39]. The absence of this feature in the two PLD samples, along with the strong presence of wurtzite peaks in diffraction, could indicate that the structure is more wurtzite than zinc blende. Similarly, the MBE sample is likely to be more zinc blende than wurtzite. Claiming that only one structure is present in the samples is not possible based on the results presented. It might be that the one wurtzite reflection seen in the MBE sample is due to stacking faults in a zinc blende structure. The stacking sequence in the [111] direction in zinc blende is ABCABC, while the [001] direction in wurtzite stacking sequence is ABAB (as explained in section 2.3). This makes the two structures very similar in these directions.

The accuracy of the 1D intensity profiles is highly dependent on how accurate the center on the diffraction image is defined. Each pixel off center will broaden

the peaks by two pixels, making it harder to separate peaks close to each other. A well centered diffraction image will place the peaks closer to the theoretical table values.

It is hard to make any claims about on film quality depending on deposition technique, due to the fact that the MBE sample has 1.5% Cr and the PLD samples has 4% Cr. Differences are seen, but there is no evidence that relates them to the deposition technique.

5.2 Spectroscopy

5.2.1 EDX

The EDX data from the five line scans all show large variations of Cr concentration over small scales. The first question might be if Cr forms metallic particles in the ZnS thin film. This is unlikely as there is no supporting evidence from BF and HAADF images or from EELS. There is also a systematic correlation between the Zn content and the Cr content. In every scan it is seen that whenever there is an increase in Cr, there is also a decrease in Zn. The concentration of S does not have these large variations. This indicates that Zn^{2+} in the ZnS lattice is substituted by Cr^{2+}.

Since ZnS is polymorphic, the varying Cr concentration could be due to the possibility of a mixture of zinc blende grains and wurtzite grains. Because of sample thickness and visibility of grains, it is hard to see if there is any relation between grains and Cr content. Even if the sample was so thin that each grain stood out really well, it would still be hard to distinguish a zinc blende grain from a wurtzite grain. Line scan 3 was done over a relatively visible grain, Fig. 4.14. The Cr concentration is lower in this grain than on either side, which could indicate Cr segregating on the grain boundary.

It is hard to confirm Cr in grain boundaries as the grains are smaller than the thickness of the specimen, meaning that there could be grains overlapping, or partly overlapping the visible grain. Judging from the BF images of PZnS:CrPV, the grains are also likely to be rounded in shape. This will also make it harder to find Cr over grain boundaries with EDX in cross section samples. Stray signal from nearby Cr will also decrease the spatial resolution of the EDX scan.

Quantification of the five scans by resulted in a Cr concentration of 4.41±0.03%, which is 0.41 percentage points more than the reported value. Since the scans show Cr variations on small scales, and the pattern is seen repeatedly, the five scans should yield a good enough statistical basis to assume that the Cr concentration found is an accurate average of the sample. There is no evidence pointing at Cr variations on larger scales than was measured in the scans. However, the Cliff-Lorimer method used to quantify the elements does not take the thickness of the specimen into account. This is despite having low loss EELS data in every

point of the scan which can be used to calculate the thickness. To improve the Cliff-Lorimer method, the thickness of the specimen should be taken into account. The sensitivity factor k_{ZnS} could also be calibrated using standard samples with a known ratio of ZnS. This work might be more suitable for a longer project. The quantification algorithm is also inaccurate when the scan goes from film to vacuum, as seen in Fig. 4.11.

5.2.2 EELS

Since there are no theoretical values for the Cr-$L_{2,3}$ fine structure, the results of this work have to be compared to similar studies. The EELS analysis is based on the method described in [35]. This article reports the energy of the L_2 and L_3 edges and L_3/L_2 for various Cr compounds spanning over all the valency states of Cr. The conclusion of the results presented in this thesis are based on comparison with this article.

The scans 2-5 was used to do the analysis. The first scan was omitted due to using experimental parameters that gave a weak fine structure signal. The four scans were split in two, first and second half of the scan. The analysis was carried out one each part. This was done to see if the valence state of Cr changed in different places of the film. Ideally, analysis should be done on individual grains. Due to the grain boundaries being hard to detect with HAADF, this was only done on one grain, Fig. 4.14. A thinner specimen with larger grains would give better conditions for this kind of analysis.

The Cr-L_3 edge was located at $577.2\,\mathrm{eV}$ and the Cr-L_2 edge at $586.1\,\mathrm{eV}$ on average. By comparing the values in Table 4.6 to the tables in Fig. B.1 and B.2 in Appendix B it is seen that the average value of the L_3 edge fits well with the values of $CrCl_2$ and Cr. The average value of the L_2 fits well with CrF_2. Cr is +II valent in both $CrCl_2$ and CrF_2 with a so-called high spin d" configuration [35]. It is likely that metallic Cr is not present. Particles of Cr have not been seen in diffraction patterns nor in BF or HAADF images. Metallic Cr could be incorporated interstitially in the ZnS lattice, but the results from EDX suggests that Cr is incorporated substitutionally. When metallic Cr is ruled out, +II valent Cr is the only explanation based on the L_2 and L_3 edges. It might be somewhat unexpected that the L_2 and L_3 values are not closer to the values of CrSe if the Cr substitutes Zn. Since Se is in the same group as S, one would expect that the bonds between the atoms are similar.

The ratio of the area under the fine structure L_3/L_2 was calculated for each part of line scans 2-4. The ratio varies between 1.6142 and 1.8799, as shown in Table 4.6. L_3/L_2 is very dependent on the width of the integration windows and also background subtraction methods. Variations in L_3/L_2 can be caused by the Fourier deconvolution method, which can cause artifacts in the data [17, p.700]. Because the Cr concentration is low in comparison to the compounds in the reference paper [35], the signal is also much weaker. A low signal to noise

ratio will make the data susceptible to artifacts when removing the background signal. Artifacts after Fourier deconvolution are seen in Fig. 3.5. The smoothing filter was applied to account for this. The values of L_3/L_2 are therefore not as accurate as the values of the L_2 and L_3 edges.

Instead of the individual L_3/L_2 values, the average value is used when comparing with the reference paper. The average value of L_3/L_2 was found to be 1.7381. By comparing this value to table B.2, it is seen that the organic +II valent Cr compounds $[(CH_3)_4C_5H]_2Cr$, $Cr_2(CH_3COO)_4 \cdot 2\,(H_2O)$ and $[(CH_3)_5C_5]_2Cr$ have similar L_3/L_2 ratios. In these compounds Cr has a low spin Cr d" configuration. Going by the individual L_3/L_2 values, Cr could also have a valence state of +I or +III. However, the L_2 and L_3 values for +I and +III valent Cr are not matching the measured values. +I and +III valent Cr is therefore ruled out.

Going by the results from EDX and EELS, it is concluded that Cr in the cross section PLD sample is +II valent.

Chapter 6

Conclusion

The morphology of three Cr-doped ZnS thin films have been characterized. Two of the samples were grown by PLD and were reported to have a Cr concentration of 4%, the third sample was grown by MBE with a reported Cr concentration of 1.5%. Bright field imaging in TEM has been used to examine the size and shape of the grains. Results show that the grains are columnar and have features of the van der Drift growth model. The crystal structure of the three samples have been investigated using diffraction patterns and 1D intensity profiles. The cross section PLD sample shows that the [111] direction in zinc blende or [001] direction in wurtzite is the preferred growth orientation. Clear differences in crystal structure is seen from diffraction patterns and 1D intensity profiles. The PLD samples both show several reflections due to wurtzite structures, while the MBE sample only shows one. An entirely unambiguous determination of crystal structure is unfortunately not possible due to many d_{hkl} values being shared between zinc blende and wurtzite. However, evidence indicates that the samples grown by PLD have a structure containing more wurtzite than zinc blende, and the MBE sample containing more zinc blende than wurtzite.

The PLD sample prepared in cross section was studied in greater detail using EDX and EELS line scans. Results from EDX show that there are large variation in Cr concentration. The Cr concentration was found to be $4.41 \pm 0.03\%$. A systematic connection between increase in Cr concentration and decrease in Zn concentration is seen. This indicates that the Cr enters substitutionally in the ZnS thin film by substituting Zn. Using EELS, the valence state of Cr has been found to be +II, thus supporting the EDX results.

Chapter 7

Further Work

The purpose of the thin films is to realize the intermediate band concept in third generation photovoltaics. The success of this is highly dependent on the microstructure of the thin film. Every grain boundary, dislocation or impurity will act as SRH recombination centers for electron-hole pairs, decreasing the efficiency of the photovoltaic conversion. The best case scenario would be to have epitaxial ZnS with the Cr distributed evenly in the thin film. It has been shown that this is not the case with the samples studied, improvement on film quality is therefore needed. Epitaxial growth of ZnS has been reported on sapphire and silicon substrates, using PLD [26]. Further work on thin film deposition to achieve epitaxial growth is recommended.

A suggestion for further work on the topic of this thesis would be to prepare cross section and plan view specimen from the sample material deposited at the same time in order to study it from both perspectives. It would also be interesting to see how ZnS:Cr would deposit on a Si substrate oriented in the [111] direction. Spectroscopy and diffraction analysis of MBE samples with the same amount of Cr as the PLD samples, would give information about the differences between PLD and MBE deposition. A closer look at distribution of Cr could be done by performing line scans over grain boundaries in a plan view specimen.

References

[1] International energy outlook 2013. `http://www.eia.gov/forecasts/ieo/world.cfm`. Accessed: 26.11.2013.

[2] Statement on climate change from 18 scientific associations. `http://climate.nasa.gov/scientific-consensus`. Accessed: 12.05.2014.

[3] The current and future consequences of global change. `http://climate.nasa.gov/effects`. Accessed: 12.05.2014.

[4] A. Luque and A. Martí. Increasing the efficiency of ideal solar cells by photon induced transitions at intermediate levels. *Physical Review Letters*, 78(26):5014–5017, 1997.

[5] Martin A. Green. *Third Generation Photovoltaics: Advanced Solar Energy Conversion*. Springer, 2003.

[6] Peter Würfel. *Physics of Solar Cells*. Wiley-VCH, 2009.

[7] W. Shockley and W.T. Read. Statistics of the recombinations of holes and electrons. *Physical Review*, 87(5):835–842, 1952.

[8] R.N. Hall. Electron-hole recombination in germanium. *Physical Review*, 87(2):387–387, 1952.

[9] D.V. Lang and C.H. Henry. Nonradiative recombination at deep levels in GaAs and GaP by lattice-relaxation multiphonon emission. *Physical Review Letters*, 35(22):1525–1528, 1975.

[10] A. Luque, A. Martí, and C. Stanley. Understanding intermediate-band solar cells. *Nature Photonics*, 6(3):146–152, 2012.

[11] K. Tanabe, D. Guimard, D. Bordel, et al. High-efficiency InAs/GaAs quantum dot solar cells by metalorganic chemical vapor deposition. *Applied Physics Letters*, 100(19), 2012.

[12] A. Luque and A. Martí. The intermediate band solar cell: Progress toward the realization of an attractive concept. *Advanced Materials*, 22(2):160–174, 2010.

[13] David B. Williams and C. Barry Carter. *Transmission Electron Microscopy Part 1: Basics*. Springer Science+Business Media, LLC, 1996.

[14] David B. Williams and C. Barry Carter. *Transmission Electron Microscopy Part 3: Imaging*. Springer Science+Business Media, LLC, 1996.

[15] Frank L. Pedrotti, Leno M.S.J. Pedrotti, and Leno S. Pedrotti. *Introduction to Optics 3rd ed.* Pearson Education, Inc., 2007.

[16] Charles Kittel. *Introduction of Solid State Physics 8th ed.* John Wiley & Sons, Inc., 2005.

[17] David B. Williams and C. Barry Carter. *Transmission Electron Microscopy Part 4: Spectrometry*. Springer Science+Business Media, LLC, 1996.

[18] R.S. Carmichael. Abundance of elements in the earth's crust and in the sea. *CRC Handbook of Chemistry and Physics*, pages 14–18, 1989.

[19] L.D. DeLoach, R.H. Page, G.D. Wilke, et al. Transition metal-doped zinc chalcogenides: Spectroscopy and laser demonstration of a new class of gain media. *IEEE Journal of Quantum Electronics*, 32(6):885–895, 1996.

[20] T. Saitoh, T. Yokogawa, and T. Narusawa. Single-crystalline epitaxial ZnS waveguides for phase matched second generation devices. *Japanese Journal of Applied Physics*, 30(4):667–671, 1991.

[21] L. Soonckindt, D. Etienne, J.P. Marchand, et al. The composition and temperature dependences of the fundamental bandgap in ZnSxSe1-x alloys. *Surface Science*, 86(0):378 – 383, 1979.

[22] The RRUFF Project. `http://rruff.info/doclib/hom/cubic.pdf`. Accessed: 07.05.2014.

[23] Connexions, crystal structure. `http://cnx.org/content/m16927/latest/`. Accessed: 04.02.2014.

[24] K.C. Sharma and Y.A. Chang. The S-Zn (sulfur-zinc) system. *Journal of Phase Equilibria*, 17(3):261–266, 1996.

[25] The RRUFF Project. `http://rruff.info/doclib/hom/wurtzite.pdf`. Accessed: 07.05.2014.

[26] Z.-J. Xin, R.J. Peaty, H.N. Rutt, et al. Epitaxial growth of high quality ZnS films on sapphire and silicon by pulsed laser deposition. *Semiconductor Science and Technology*, 14(8):695–698, 1999.

[27] H.M. Smith and A.F. Turner. Vacuum deposited thin films using a ruby laser. *Applied Optics*, 4(1):147–148, 1965.

[28] H.-U. Krebs, M. Weisheit, J. Faupel, et al. Pulsed Laser Deposition (PLD) – A versatile thin film technique. In *Advances in Solid State Physics*, volume 43 of *Advances in Solid State Physics*, pages 505–518. Springer Berlin Heidelberg, 2003.

[29] Robert Eason. *Pulsed Laser Deposition of Thin Films.* Wiley & Sons Inc., 2007.

[30] Ben G. Streetman and Sanjay Kumar Banerjee. *Solid State Electronic Devices 6th ed.* Pearson Education Inc., 2006.

[31] Unpublished research by Mohammadreza Nematollahi. Date: 2013 and 2014.

[32] Gatan Digital Micrograph. `http://www.gatan.com/products/software/`. Accessed: 08.05.2014.

[33] Script for Digital Micrograph, SADP rotational average. `http://donation.tugraz.at/dm/source_codes/158`. Accessed: 12.05.2014.

[34] Script for Digital Micrograph, SADP define centre. `http://donation.tugraz.at/dm/source_codes/156`. Accessed: 12.05.2014.

[35] T.L. Daulton and B.J. Little. Determination of chromium valence over the range Cr(0)–Cr(VI) by electron energy loss spectroscopy. *Ultramicroscopy*, 106(7):561 – 573, 2006.

[36] E. Spiecker, V. Radmilovic, and U. Dahmen. Quantitative TEM analysis of 3-d grain structure in CVD-grown SiC films using double-wedge geometry. *Acta Materialia*, 55(10):3521 – 3530, 2007.

[37] Unpublished research by Xiaodong Yang and Peter Kusterle. Date: 2013.

[38] W. L. Garret, G. Ruban, and F. Williams. Anisotropy and twinning in cubic zinc sulfide crystals. *Journal of Physics and Chemistry of Solids*, 43(6):497 – 500, 1982.

[39] L. C. Qin, D. X. Li, and K. H. Kuo. An HREM study of the defects in ZnS. *Philosophical Magazine A*, 53(4):543–555, 1986.

[40] M. Adamik, P.B. Barna, and I. Tomov. Columnar structures in polycrystalline thin films develiped by competitive growth. *Thin Soild Films*, 317:64 – 68, 1998.

[41] A. van der Drift. *Philips Res. Rep.*, 22(267), 1967.

[42] Web Electron Microscopy Applications Software (WebEMAPS). `http://emaps.mrl.uiuc.edu/default.asp`. Accessed: 23.05.2014.

Appendix A

Calculating L_3/L_2

Below is the script used for doing background subtraction and calculating L_3/L_2 for the EELS analysis.

```
# -*- coding: utf-8 -*-
"""
Created on Mon May 5 20:26:23 2014

@author: Eivind
"""

from __future__ import division
import numpy as N


#=======================================================
#
# An EELS background correction script
#
# Instructions:
# A two column .txt file containing the EELS data is required
# A power fit subtraction must have been applied beforehand
# Change code where indicated
#=======================================================

starteV = # Energy of channel 1 in EELS data
dispersion = # Energy width of channels in EELS detector
xdata = N.zeros(2048)
ydata = N.zeros(2048)
counter = 0
negativecounter = 0
tobesnitt = 0

integrationboxwidth = 50
iboxstart = integrationboxwidth//2
iboxend = (integrationboxwidth//2) - 1

L3peak = # Insert channel at peak of L3
L3peakstart = L3peak-iboxstart
```

```
L3peakend = L3peak+iboxend

L2peak = # Insert channel at peak of L2
L2peakstart = L2peak - iboxstart
L2peakend = L2peak + iboxend

boxstart = L2peak + 48
boxend = boxstart + 20
box = boxend - boxstart

for line in open("mydata.txt"): # Insert filename of data file
    columns = line.split("\t")
    xdata[counter] = columns[0] # Column 1 in mydata.txt
    ydata[counter] = columns[1] # Column 2 in mydata.txt
    counter += 1

for i in range(boxstart,boxend):
    temp3 = ydata[i]
    tobesnitt = tobesnitt + temp3
snitt = tobesnitt/box

# Change "ratiofactor" before every iteration, starting at 1/2
ratiofactor = 1/2

for i in range(L2peak,counter):
    ydata[i] = ydata[i] - snitt

for i in range(L3peak,L2peak):
    ydata[i] = ydata[i] - snitt - snitt/(1+ratiofactor)

for i in range(0,counter):
        if ydata[i] < 0:
            ydata[i] = 0

f = open("mydatacorrected.txt", "w") # Creates a file for results
for i in range(0,counter):
    temp = str(xdata[i])
    temp2 = str(ydata[i])
    f.write(temp + '\t' + temp2 + '\n')
f.close

# Trapezoidal method:
L3area = 0
for i in range (L3peakstart,L3peakend):
    L3area = L3area + (xdata[i+1]-xdata[i])*(ydata[i]+ydata[i+1])/2

L2area = 0
for i in range (L2peakstart,L2peakend):
    L2area = L2area + (xdata[i+1]-xdata[i])*(ydata[i]+ydata[i+1])/2

print "====== Results =====" + "\n"
print "L3/L2 ratio: " + str(L3area/L2area)
print "L3 peak at [eV]: " + str(L3peak*dispersion + starteV)
print "L2 peak at [eV]: " + str(L2peak*dispersion + starteV)
```

Appendix B

Cr-L$_{2,3}$ Fine Structure

T.L. Daulton, B.J. Little / Ultramicroscopy 106 (2006) 561–573

Table 3
Cr-L adsorption edge ratios

Compound	L$_3$/L$_2$ integrated ratio			
	Background method 1 Pearson et al. (1993) [86]		Background method 2 Zero-slope two step	
	$n = 1$	$n = 10$	$n = 1$	$n = 10$
Cr$_{23}^{0}$C$_6$ $^{\text{cLS}}$	1.324 ± 0.007	1.315 ± 0.007	1.511 ± 0.003	1.498 ± 0.003
Cr^0(CO)$_6$ $^{\text{LS}}$	1.419 ± 0.020	1.416 ± 0.019	1.525 ± 0.007	1.520 ± 0.007
Cr^0 $^{\text{cLS}}$	1.389 ± 0.003	1.377 ± 0.003	1.540 ± 0.003	1.525 ± 0.003
(C$_6$H$_6$)$_2$Cr^{I}I $^{\text{cLS}}$	1.631 ± 0.011	1.620 ± 0.010	1.807 ± 0.007	1.798 ± 0.006
[(CH$_3$)$_4$C$_5$H]$_2$Cr^{II} $^{\text{LS}}$	1.612 ± 0.012	1.605 ± 0.012	1.723 ± 0.004	1.715 ± 0.004
Cr$_3^{II}$(CH$_3$COO)$_4$·2(H$_2$O) $^{\text{LS}}$	1.633 ± 0.007	1.630 ± 0.006	1.729 ± 0.003	1.720 ± 0.002
[(CH$_3$)$_5$C$_5$]$_2$Cr^{II} $^{\text{LS}}$	1.620 ± 0.017	1.616 ± 0.016	1.762 ± 0.004	1.757 ± 0.003
Cr^{II}Se $^{\text{cHS}}$	1.899 ± 0.022	1.895 ± 0.022	2.004 ± 0.013	2.004 ± 0.013
Cr^{II}Cl$_2$ $^{\text{HS}}$	2.311 ± 0.044	2.327 ± 0.045	2.178 ± 0.017	2.184 ± 0.017
Cr^{II}F$_2$ $^{\text{HS}}$	2.386 ± 0.025	2.400 ± 0.026	2.240 ± 0.014	2.246 ± 0.014
Cr^{III}PO$_4$·4H$_2$O	1.490 ± 0.004	1.489 ± 0.005	1.554 ± 0.003	1.546 ± 0.003
KCr^{III}(SO$_4$)$_2$·12H$_2$O	1.508 ± 0.009	1.504 ± 0.009	1.565 ± 0.005	1.559 ± 0.005
Cr^{III}Cl$_3$	1.589 ± 0.008	1.585 ± 0.008	1.644 ± 0.003	1.638 ± 0.003
(Fe,Mg)(Cr^{III},Al,Fe)$_2$O$_4$	1.644 ± 0.005	1.638 ± 0.004	1.653 ± 0.002	1.646 ± 0.002
NdCr^{III}O$_3$	1.619 ± 0.011	1.616 ± 0.009	1.684 ± 0.007	1.675 ± 0.007
LaCr^{III}O$_3$	1.604 ± 0.005	1.600 ± 0.005	1.711 ± 0.004	1.704 ± 0.004
Cr^{III}(CH$_3$COO)$_7$(OH)$_2$	1.624 ± 0.007	1.618 ± 0.006	1.715 ± 0.002	1.709 ± 0.002
Cr$_2^{III}$O$_3$	1.679 ± 0.013	1.671 ± 0.012	1.720 ± 0.006	1.712 ± 0.005
Cr$_2^{IV}$O$_2$	1.484 ± 0.002	1.478 ± 0.002	1.556 ± 0.002	1.548 ± 0.002
NdCr^{V}O$_4$	1.398 ± 0.006	1.387 ± 0.005	1.426 ± 0.005	1.414 ± 0.004
PbCr^{VI}O$_4$	1.368 ± 0.006	1.355 ± 0.006	1.381 ± 0.005	1.370 ± 0.005
K$_2$Cr$_2^{VI}$O$_7$	1.397 ± 0.006	1.387 ± 0.006	1.418 ± 0.006	1.408 ± 0.006
K$_2$Cr^{VI}O$_4$	1.416 ± 0.005	1.405 ± 0.005	1.484 ± 0.004	1.474 ± 0.004
Na$_2$Cr^{VI}O$_4$	1.498 ± 0.008	1.484 ± 0.008	1.486 ± 0.006	1.475 ± 0.006

cLS—conjectured low spin Cr d^n configuration.
LS—low spin Cr d^n configuration.
cHS—conjectured high spin Cr d^n configuration.
HS—high spin Cr d^n configuration.

Figure B.1: L$_3$/L$_2$ for Cr compounds. Adapted from [35].

Table 1
Cr-L$_3$ (2p$_{3/2}$) and Cr-L$_2$ (2p$_{1/2}$) adsorption-edges: EELS—edge maxima[a]

Compound	Formal valence	Cr-L$_3$ (2p$_{3/2}$) (eV)	Cr-L$_2$ (2p$_{1/2}$) (eV)	Reference
Cr$_{20}$Au$_{80}$ [cLS]	0	570.6	580.2	Pease et al. (1986)[b] [88]
Cr [cLS]	0	573.6	582.1	Pease et al. (1986)[b] [88]
		575.5 ± 1.1	584.0 ± 1.1	Leapman et al. (1982)[c,d,g] [81]
		577.18 ± 0.02	585.79 ± 0.02	This study
Cr$_{23}$C$_6$ [cLS]	0	578.03 ± 0.05	586.40 ± 0.03	This study
Cr(CO)$_6$ [LS]	0	579.06 ± 0.07	587.34 ± 0.08	This study
(C$_6$H$_6$)$_2$CrI [cLS]	I	576.87 ± 0.03	585.97 ± 0.04	This study
CrSe [cHS]	II	576.65 ± 0.05	585.60 ± 0.04	This study
CrF$_2$ [HS]	II	576.78 ± 0.03	586.15 ± 0.03	This study
CrCl$_2$ [HS]	II	577.11 ± 0.04	586.66 ± 0.04	This study
[(CH$_3$)$_5$C$_5$]$_2$Cr [LS]	II	578.35 ± 0.02	586.83 ± 0.03	This study
[(CH$_3$)$_4$C$_5$H]$_2$Cr [LS]	II	578.43 ± 0.04	586.77 ± 0.03	This study
Cr$_2$(CH$_3$COO)$_4$ · 2H$_2$O [LS]	II	578.55 ± 0.03	586.95 ± 0.03	This study
Cr$_2$O$_3$	III	577.1 ± 1.1	584.7 ± 1.1	Leapman et al. (1982)[c,d,g] [81]
		578.3	586.4	Krivanek and Paterson (1990)[e,g] [89]
		578.81 ± 0.03	587.17 ± 0.03	This study
		580.6 ± 0.3	588.7 ± 0.3	Suzuki and Tomita (1997)[b] [90]
CrCl$_3$	III	578.13 ± 0.02	586.61 ± 0.02	This study
Cr$_3$(CH$_3$COO)$_7$(OH)$_2$	III	578.47 ± 0.02	586.81 ± 0.02	This study
LaCrO$_3$	III	578.71 ± 0.02	587.16 ± 0.03	This study
(Fe,Mg)(Cr,Al,Fe)$_2$O$_4$	III	578.89 ± 0.02	587.24 ± 0.02	This study
		579.8 ± 0.2	587.8 ± 0.2	Garvie et al. (1994)[f,g] [91]
NdCrO$_3$	III	579.35 ± 0.03	587.68 ± 0.03	This study
Ca$_{1.1}$(Cr,Fe,Mg)$_4$(SiAl)$_{8^-}$, (Si,Al)$_8$O$_{20}$(OH)$_4$ · nH$_2$O	III	579.7 ± 0.2	587.9 ± 0.2	Garvie et al. (1994)[f,g] [91]
CrPO$_4$ · 4H$_2$O	III	579.74 ± 0.06	588.57 ± 0.05	This study
KCr(SO$_4$)$_2$ · 12H$_2$O	III	579.77 ± 0.04	588.18 ± 0.08	This study
CrO$_2$	IV	579.70 ± 0.03	587.83 ± 0.03	This study
		581.8 ± 0.3	589.6 ± 0.3	Suzuki and Tomita (1997)[b] [90]
NdCrO$_4$	V	580.43 ± 0.03	589.05 ± 0.03	This study
K$_2$CrO$_4$	VI	581.77 ± 0.02	590.41 ± 0.02	This study
PbCrO$_4$	VI	581.85 ± 0.07	590.34 ± 0.06	This study
		582.1 ± 0.2	590.7 ± 0.2	Garvie et al. (1994)[f,g] [91]
Na$_2$CrO$_4$	VI	582.26 ± 0.03	590.77 ± 0.03	This study
K$_2$Cr$_2$O$_7$	VI	582.83 ± 0.03	591.35 ± 0.05	This study
		583.6 ± 0.3	592.3 ± 0.3	Suzuki and Tomita (1997)[b] [90]

cLS—conjectured low spin Cr d^n configuration.
LS—low spin Cr d^n configuration.
cHS—conjectured high spin Cr d^n configuration.
HS—high spin Cr d^n configuration.
[a]EELS L-edge peak positions are calibrated to NiO Ni-L$_3$ maxima at 855.0 eV.
[b]Energy calibration not reported. Although the L-edge maxima cannot be directly compared to our study, the relative energy differences in L-edge maxima between specimens from the same study can be compared to our study.
[c]EELS L-edge onsets reported in reference, however L-edge maxima are shown here.
[d]After recalibrating the EELS NiO Ni-L$_3$ edge maximum to 855.0 from 856.3 eV (determined to have been used in reference).
[e]After recalibrating the EELS NiO Ni-L$_3$ edge maximum to 855.0 from 852.75 eV used in reference.
[f]After recalibrating the EELS NiO Ni-L$_3$ edge maximum to 855.0 from 853.2 eV used in reference.
[g]Recalibrated peak position = old peak position × (old Ni-L$_3$ edge maximum)/855.0 eV.

Figure B.2: Cr-L$_2$ and Cr-L$_3$ ionization edges for Cr compounds. Adapted from [35].